Microstructure in SOFC: electrochemical simulations and experiments

Zhang, Xiaoqiang

2023

Document Version:
Publisher's PDF, also known as Version of record

Microstructure in SOFC:

electrochemical simulations and experiments

XIAOQIANG ZHANG
DEPARTMENT OF ENERGY SCIENCES | FACULTY OF ENGINEERING | LUND UNIVERSITY

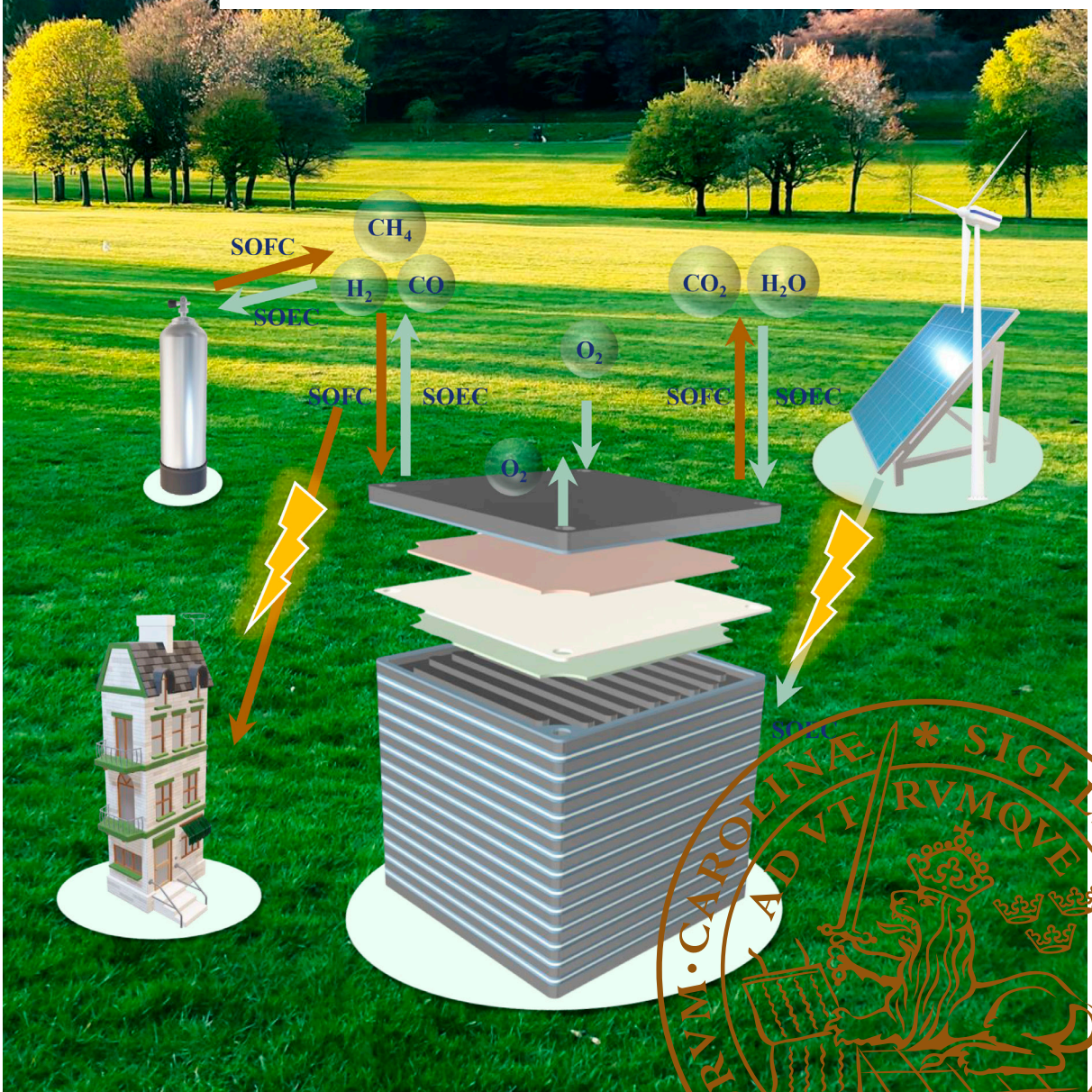

Microstructure in SOFC: electrochemical simulations and experiments

Microstructure in SOFC: electrochemical simulations and experiments

by Xiaoqiang Zhang

LUND
UNIVERSITY

Thesis for the degree of Doctor of Philosophy
Thesis advisors: Docent. Martin Andersson, Docent. Lei Wang, Dr. Himani Garg
Faculty opponent: Ass.Prof. Pablo A. García-Salaberri, University Carlos III of Madrid, Spain

To be presented, with the permission of the Faculty of Engineering of Lund University, for public criticism at KC:A on Friday, the 16th of June 2023 at 10:15.

Organization
Lund University
Department of Energy Sciences
Box 118
SE–221 00 LUND
Sweden

Document name
DOCTORAL DISSERTATION

Date of disputation
2023-06-16

Sponsoring organisation
China Scholarship Council (CSC)
Royal Physiographic Society in Lund

Author(s)
Xiaoqiang Zhang

Title and subtitle
Microstructure in SOFC: electrochemical simulations and experiments

Abstract

Solid oxide fuel cells (SOFCs) are highly efficient and environmentally friendly power sources that convert chemical energy directly into electricity and heat, without the need for combustion. Despite their many benefits, the performance and durability of SOFCs heavily depend on the quality of their porous anode and cathode components. There are significant challenges with regard to their commercialization due to the potential failure and degradation of their anode and cathode components. Optimizing SOFC electrodes requires obtaining critical microstructure parameters and understanding their impact on the overall performance. This can be achieved through advanced tomography techniques and fully coupled Multiphysics simulations, which provide insights into the quality of the electrode and the complex electrochemical processes that occur within it.

In this thesis, experiments were conducted to investigate different anode microstructure impacts on SOFC performance through electrochemical analysis. Besides, 2D microstructure tomography was obtained to construct real 3D volumes. Based on the tomography information, the porosity and tortuosity of the porous electrode were calculated and compared. Different tortuosity calculation methods were compared to obtain values used for Multiphysics simulations.

A fully coupled Multiphysics model was constructed step by step. Firstly, the electrochemical kinetic models are compared based on the Butler-Volmer equations. Secondly, different diffusion models are compared with and without Knudsen diffusion. Based on the 3D Multiphysics CFD model, the microstructure parameters' impact on the SOFC performance was studied. Meanwhile, a SOFC model based on different sealant materials was constructed to investigate the overall thermal stress distribution. Thermal stress at an electrode/electrolyte interface was also modelled and analyzed. The results showed that the interface contact mode and the geometry size of the SOFC component significantly impacted the thermal stress distribution and its values.

In summary, the experiment analysis findings emphasize optimizing the microstructure design to balance gas diffusion, charge transport, and electrochemical reactions. The fully coupled Multiphysics models can be used for further SOFC design, regarding internal transport processes and mechanical stability. In general, this thesis has made contributions to the field of SOFCs.

Key words
Solid oxide fuel cell, Electrochemical impedance spectroscopy, 3D reconstruction, Tortuosity, Electrochemical kinetics, Multiphysics, Thermal stress

Classification system and/or index terms (if any)

Supplementary bibliographical information

Language
English

ISSN and key title
0282-1990

ISBN
978-91-8039-729-2 (print)
978-91-8039-730-8 (pdf)

Recipient's notes

Number of pages
187

Price

Security classification

Signature _____ Date 2023-05-16

Microstructure in SOFC: electrochemical simulations and experiments

by Xiaoqiang Zhang

LUND
UNIVERSITY

A doctoral thesis at a university in Sweden takes either the form of a single, cohesive research study (monograph) or a summary of research papers (compilation thesis), which the doctoral student has written alone or together with one or several other author(s).

In the latter case the thesis consists of two parts. An introductory text puts the research work into context and summarizes the main points of the papers. Then, the research publications themselves are reproduced, together with a description of the individual contributions of the authors. The research papers may either have been already published or are manuscripts at various stages (in press, submitted, or in draft).

Cover illustration front: Illustration of SOEC/SOEC stack, which can be used to generate electricity or produce fuels.

Cover illustration back: 3D reconstructed anode material of SOFC with pores in blue and solid in green.

Funding information: The thesis work was financially supported by the Chinese Scholarship Council (CSC), Royal Physiographic Society in Lund.

Faculty of Engineering, Department of Energy Sciences

ISBN: 978-91-8039-729-2 (print)
ISBN: 978-91-8039-730-8 (pdf)
ISSN: 0282-1990
ISRN: LUTMDN/TMHP-23/1174-SE

Printed in Sweden by Media-Tryck, Lund University, Lund 2023

A person can do nothing better than to eat and drink and find satisfaction in their own toil. This too, I see, is from the hand of God, for without him, who can eat or find enjoyment? (Ecclesiastes 2:24 NIV)

Contents

List of publications

I **Thermal stress analysis at the interface of cathode and electrolyte in solid oxide fuel cells**
Xiaoqiang Zhang, Siqi Yu, Minkang Wang, Shuyue Dong, Joseph Parbey, Ting Shuai Li*, Martin Andersson
International Communications in Heat and Mass Transfer, 2020, 118: 104831.
https://doi.org/10.1016/j.icheatmasstransfer.2020.104831

II **Numerical simulation of solid oxide fuel cells comparing different electrochemical kinetics**
Xiaoqiang Zhang, Lei Wang, Mayken Espinoza, Tingshuai Li, Martin Andersson*
International Journal of Energy Research, 2021, 45(9): 12980-12995.
https://doi.org/10.1002/er.6628

III **Parametric study for electrode microstructure influence on SOFC performance**
Xiaoqiang Zhang, Mayken EspinozaTing, Ting Shuai Li, Martin Andersson*
International Journal of Hydrogen Energy, 2021, 46(75): 37440-37459.
https://doi.org/10.1016/j.ijhydene.2021.09.057

IV **Analysing Tortuosity for Solid Oxide Fuel Cell Anode Material - Experiments and Modeling**
Xiaoqiang Zhang*, Danan Yang, Aaron Naden, Min Xu, Ting Shuai Li, John T. S. Irvine, Martin Andersson*
Journal of The Electrochemical Society, 2023
Under review

V **High gas tightness ZrO_2 doped silicate glass sealant with low thermal stress for solid oxide fuel cells**
Mengyuan Guo, **Xiaoqiang Zhang**$^{\#}$, Ying Li, Martin Andersson, Zhibin Yang*, Suping Peng
Ceramic International, 2023, 49(12), 19708-19716
https://doi.org/10.1016/j.ceramint.2023.03.088

Acknowledgements

This research was conducted at Lund University's Faculty of Engineering, in the Department of Energy Sciences' Division of Heat Transfer. I would like to express my gratitude to the China Scholarship Council (CSC) and the Stig Borglin Scholarship from the Royal Physiographic Society in Lund for their generous support.

My heartfelt thanks go to Docent. Martin Andersson, my main supervisor, for his invaluable guidance and support throughout my PhD studies. I am also grateful to my co-supervisor, Docent. Lei Wang, and Dr. Himani Garg, Prof. Tingshuai Li, Dr. Mayken Espinoza, for their assistance and feedback. Additionally, I am indebted to Dr. Min Xu from Tsinghua University for his assistance, guidance, and stimulating discussions.

I would like to acknowledge the Department's administrative team, including Prof. Magnus Genrup, Catarina Lindén, Isabelle Frej, and division head Prof. Christer Fureby, for their kind help and support. I am also grateful for the insightful courses of Prof. Christer Fureby, Prof. Johan Revstedt, Docent. Hesameddin Fatehi, Docent. Rixin Yu, and Dr. Narmin Hushmandi.

I extend my thanks to Prof. John Irvine from the University of St Andrews for inviting me to visit the JTSI group and providing me with invaluable insights into advanced energy materials. My colleagues and friends from both the Department of Energy Sciences and the JTSI Group have been a constant source of invaluable support throughout my academic journey.

I would also like to express my gratitude to Zhen Cao and Yong Li, who have been role models in both academics and life. I am also grateful to Feng Zhang, Hongwei Mao, Bolun Zhang, and others who have spent time with me for discussions and recreation. Thanks to Danan Yang, Shuo Yang, Deiquan Xu, Zhan Liu, and Zhe Xing for their help and camaraderie.

Thanks to Miao Zhang, Leilei Xu, Shijie Xu, Huaduo Gu, Miao Yang, Heng Hu, Sheng Feng, and others for either insightful discussions, travelling exercises, and joyful times. Thanks to Gustav Karlsson, Arvid Åkerblom, Rasmus Robertsson, Alessandro Ercole, Guillaume Sahut, Thommie Nilsson, Marcus Hothar, Michael Bertsch, Morteza Mousavi, and others for their interesting discussions and department activities.

Furthermore, I would like to express my appreciation to Damiano Bonaccorso, Jair Triana Pequeno, Gavin Irvine, Shangshang Zuo, Chengzhi Sun,

Xinyu Liu, Zipei Wan, and others who have helped me, had discussions with me, and shared enjoyable moments during my stay at the JTSI Group at the University of St Andrews.

I also thank my fellowship at Lund: Zehan Yao and Yue Wu, Yu-Chen Cheng, Yang Fu, Pinxi Chen, Yizhen Wang, and others for countless joyful times to study and accompany.

Finally, I would like to extend my heartfelt gratitude to my family: my father, Xuexi Zhang (张学喜), my mother, Aizhen Niu (牛爱珍), and my brother, Zhiqiang Zhang (张智强). Their unwavering support, encouragement, and love have been the driving force behind my academic journey. Their sacrifices, selflessness, and dedication to my success have been invaluable, and I cannot express my appreciation enough. My heart is brimming with an enduring love for the one I cherish, transcending time, space, and even life itself.

Popular Science Summary

Since the discovery of fire during the primitive era, the energy extraction process has remained largely unchanged. Combustion of fuels has been widely used for transportation, electricity generation, and residential applications, which brings air pollution and large heat losses. However, solid oxide fuel cells (SOFCs) offers an innovative and sustainable alternative, which electronically converts the energy in the fuel into electricity with efficiency of 65% without combustion processes. The operating temperature is between 700 and 1000 ° C, which can be used for heating, driving steam turbines, resulting in significantly higher efficiency compared to direct fuel combustion. In addition, various fuels can be used, which offers a clean, quiet, source of energy with low emissions and can help to mitigate the environmental impact of conventional energy sources. The benefits of SOFCs technology extend to a wide range of applications, including transportation, stationary power plants, and micro-combined heat and power systems. Overall, SOFC technology has the potential to revolutionize the way we generate and use energy, and it is a promising solution to the challenges we face in achieving sustainable energy production and consumption.

The concept of SOFCs can be traced back to the 19th century when scientists discovered water electrolysis, a process that produces hydrogen (H_2) and oxygen (O_2). Subsequently, scientists found that the reverse process of recombining H_2 and O_2 could generate electrical current. A SOFC consists of an electrolyte sandwiched between an anode and a cathode, which separate the H_2 and O_2 on the anode and cathode sides, respectively. During the operation, water is generated on the anode side while electrons are produced on the cathode side, generating electricity with heat as by-product. When connected to a current source, a SOFC can also produce H_2 and O_2 in the cathode and anode by providing water and air, thereby highlighting its potential for power supply and energy storage.

The commercial viability of SOFCs depends on achieving a lifetime of 90,000 hours. However, the high operating temperature of SOFCs presents significant challenges to the mechanical and chemical stability of their cell components. These challenges are particularly pronounced in the anode and cathode, which have complex porous microstructures that significantly impact the SOFC's performance and lifetime. Thus, accurately calculating the porous electrode parameters and understanding their influence on the overall performance of the SOFC are essential steps to address these stability and lifetime-related issues. Finally, optimization of these parameters

is necessary to enhance the stability and durability of the SOFC, which is critical for its widespread commercial success.

The microstructure of the porous electrode can be controlled and characterized by different means. One of the method is to change the electrode composition, followed by cell test and 3D microstructure reconstruction. Besides, the processes in the SOFC have Multiphysics nature, which involves heat, species, momentum, and charge transfer. Multiphysics simulation of SOFC can reveal the internal process that the experimental method is hard to capture. Therefore, the thesis is broadly divided in two parts: experiment and Multiphysics simulation.

In the experiment, we aimed to evaluate the electrochemical performance of SOFCs with different anode microstructures. After the test, we conducted a 3D reconstruction of the microstructure to calculate the relevant gas transport-related microstructure parameters. Before performing the Multiphysics simulation, we compared and assessed various electrochemical kinetics and species diffusion models. Next, we utilized Multiphysics models to investigate how the microstructure parameters affect the electrical and thermal properties of SOFCs. Furthermore, Thermal stress is a critical concern as uneven distribution can lead to accelerated SOFC ageing and mechanical failure beyond the stress limits. Therefore, we analyzed the thermal stress distribution at both micro and macro scales of the SOFCs to gain a better understanding of this phenomenon. By comprehensively examining the electrochemical performance, microstructure parameters, and thermal stress distribution of SOFCs, we can better understand their behaviour and work towards optimizing their design and performance.

The thesis also sheds light on the crucial role of microstructure in determining the electrical performance of SOFCs, as evidenced by the calculation of tortuosity and subsequent simulations. These findings highlight the need to optimize microstructure design to achieve a balance between gas diffusion, charge transport, and electrochemical reactions. Besides, this PhD thesis has made contributions to the field of SOFCs by enhancing our understanding of electrochemical reaction kinetics models and diffusion models, and their role in developing accurate Multiphysics models for designing high-performance SOFCs.

Abstract

Solid oxide fuel cells (SOFCs) are highly efficient and environmentally friendly power sources that convert chemical energy directly into electricity and heat, without the need for combustion. Despite their many benefits, the performance and durability of SOFCs heavily depend on the quality of their porous anode and cathode components. There are significant challenges with regard to their commercialization due to the potential failure and degradation of their anode and cathode components. Optimizing SOFC electrodes requires obtaining critical microstructure parameters and understanding their impact on the overall performance. This can be achieved through advanced tomography techniques and fully coupled Multiphysics simulations, which provide insights into the quality of the electrode and the complex electrochemical processes that occur within it.

In this thesis, experiments were conducted to investigate different anode microstructure impacts on SOFC performance through electrochemical analysis. Besides, 2D microstructure tomography was obtained to construct real 3D volumes. Based on the tomography information, the porosity and tortuosity of the porous electrode were calculated and compared. Different tortuosity calculation methods were compared to obtain values used for Multiphysics simulations.

A fully coupled Multiphysics model was constructed step by step. Firstly, the electrochemical kinetic models are compared based on the Butler-Volmer equations. Secondly, different diffusion models are compared with and without Knudsen diffusion. Based on the 3D Multiphysics CFD model, the microstructure parameters' impact on the SOFC performance was studied. Meanwhile, a SOFC model based on different sealant materials was constructed to investigate the overall thermal stress distribution. Thermal stress at an electrode/electrolyte interface was also modelled and analyzed. The results showed that the interface contact mode and the geometry size of the SOFC component significantly impacted the thermal stress distribution and its values.

In summary, the experiment analysis findings emphasize optimizing the microstructure design to balance gas diffusion, charge transport, and electrochemical reactions. The fully coupled Multiphysics models can be used for further SOFC design, regarding internal transport processes and mechanical stability. In general, this thesis has made contributions to the field of SOFCs.

Nomenclature

Abbreviations

2/3D	two/three dimensional
I	Identity matrix
AFCs	alkaline fuel cells
APU	auxiliary power unit
BV	Butler Volmer
CFD	computational fluid dynamics
CP1,2	composition 1, 2
CT	computational tomography
CTE	coefficient of thermal expansion
DRT	distribution of relaxation times, s
EC	equivalent circuit
EIS	electrochemical impedance spectroscopy
FIB	focused ion beam
IAE	interface of anode/electrolyte
ICE	interface of cathode/electrolyte
IVP	current voltage and power curve
LTE	local temperature equilibrium
LTNE	local temperature no-equilibrium
M	molar mass, kg/mol
MCFCs	molten carbonate fuel cells
MSR	methane steam reforming
OCV	open circuit voltage
PAFCs	phosphoric acid fuel cells
PEMFC	polymer electrolyte fuel cell
Re	Reynolds number
SATP	standard ambient temperature and pressure
SEM	scanning electron microscopy
SOEC	solid electrolyzer cell
SOFCs	solid oxide fuel cells
TPBs	three phase boundaries
V	volume fraction
WGSR	water gas shift reaction

Subscripts and superscript

i, j	species i, j
0	standard condition
a/c	anode, cathode
act	activation
conc	concentration
eff	effective
f	fluid
g	gas
l	ionic
l	liquid
ohm	ohmic
s	electronic

Physical constant

F	Faraday constant, 9.6×10^4 C/mol
k_B	Boltzmann constant, 1.38×10^{-23} J/K
R	gas constant, 8.314 J/(K·mol)

Chemicals

CH_4	methane
CO	carbon monoxide
CO_2	carbon dioxide
Cr	chromium
e^-	electron
H^+	proton
H_2	hydrogen
H_2O	water
H_2S	hydrogen sulfide
LSCF	lanthanum strontium cobalt ferrite
LSM	lanthanum strontium manganite
Ni	nickel
O^{2-}	oxygen ion
O_2	oxygen
OH^-	hydroxide
YSZ	yttria-stabilized zirconia

Variables

α	transfer coefficient, -
η	overpotential, V
κ	permeability, m^2
μ	dynamic viscosity, Pa·s
ω	mass fraction, -
Ω_D	collision integral for gas diffusion
ϕ	potential, V
ρ	density, kg/m^3
σ	charge conductivity, S/m
$\sigma_{i,j}$	characteristic length of gas i, j
τ	tortuosity, -
ε	porosity

i	current density, A/m^2
d	driving force, 1/m
J	mass flux, $kg/(m^2 \cdot s)$
K	stress tensor, N/m^2
u	velocity vector, m/s
a_v	active specific areal, m^2/m^3
c	molar concentration, mol/L
c_p	heat capacity act constant pressure, J/K
D	diffusion coefficient, m^2/s
E	voltage, V
$E_{a/c}$	activation energy for anode and cathode, kJ/mol
G	Gibb's free energy, J
H	enthalpy, J/mol
I	current, A
k	pre-exponential factor of exchange current density
k	thermal conductivity, $W/(m \cdot K)$
n	number of electron, -
P	power, W
p	pressure, Pa
Q	heat, J
R	resistance, Ω
R,Q_m	mass source or sink of species m, $kg/(m^3 \cdot s)$
S	entropy, J/K
T	temperature, K
x	mole fraction, -

Chapter 1

Introduction

1.1 Background

As of 2022, the average global energy consumption per capita stands at 20,993 kilowatt-hours, and this figure is expected to continue rising as energy demand increases[1]. Fossil fuels as the main energy source accounted for over 80% of primary energy usage, but their reserves and production levels are limited. Moreover, only 36 countries are classified as developed economies, while the remaining nations are still striving for economic growth. These developing countries, which comprise 80% of the world's population according to the United Nations Department of Economic and Social Affairs Analysis, represent a significant driver of global energy demand[2]. Based on current consumption rates, coal, oil, and gas reserves can only meet human needs for 139, 54, and 49 years, respectively[3,4]. The recent energy crisis in Europe, caused by Russia's invasion of Ukraine, has led to increased efforts to ensure energy security, as stated by the Council of the European Union[5]. Furthermore, fossil fuel combustion, which is the primary method of modern usage, significantly contributes to air pollution and greenhouse gas emissions, such as CO_2, meanwhile with limited efficiency. To meet the Paris Agreement's goal of achieving net-zero emissions by 2050, CO_2 emissions must be reduced to 23 gigatonnes (Gt) by 2030. Under the Net Zero Emissions scenario, the projected global average temperature increase by 2100 is less than 1.5 °C[6]. However, energy-related CO_2 emissions rebounded to 36.6 Gt in 2021 accounting for the largest-ever annual rise, presenting significant challenges in meeting these targets in the near future.

Given the current reality of dwindling fossil fuel reserves and rising carbon emissions, shifting towards a more sustainable, affordable, and cleaner energy solution is natural. This objective can be achieved by adopting renewable energy sources such as solar[7], wind[8], hydro-power[9], and fusion[10] energy. Additionally, improving the efficiency of the way we use existing primary energies with low emissions, such as exploring alternative fuels[11] and utilizing fuel cells[12]. Among these solutions, solid oxide fuel cells (SOFCs) have drawn significant attention as an effective means to reduce emissions and improve efficiency.

SOFCs are highly advanced energy conversion devices that can convert the chemical energy in fuels directly into electricity and heat without the need for combustion. The acronym SOFC is derived from the solid ceramic oxide electrolyte that conducts oxygen ions (O^{2-}). These devices can operate at high temperatures ranging from 700 to 1000 °C, allowing them to use a wide range of fuels, such as H_2, CH_4, methanol, biomass, carbon, and NH_3. They also provide high theoretical electrical efficiency of up to 65% (assuming liquid water generation) and a high-quality heat source. Moreover, SOFCs are highly scalable, ranging from kilo Watts (kW) to Mega Watts (MW) power output, and their versatility makes them suitable for various applications, such as domestic power stations, auxiliary power units (APUs) in vehicles, and stationary power plants in power grids. In addition to their high efficiency and scalability, SOFCs can also function as electrolyzers, enabling the conversion of electricity into fuels, which can be used for CO_2 capture and conversion[13].

The outstanding features of SOFCs position them as one of the viable solutions for the pressing demand for sustainable and clean energy sources. With ongoing research and development, SOFCs have the potential to revolutionize the energy industry and play a critical role in the transition towards a near-zero CO_2 emission and sustainable future.

1.2 State of art

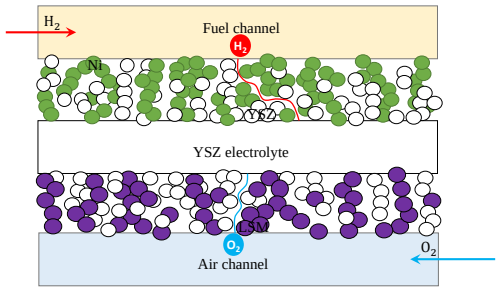

Figure 1.1: Schematic of unit SOFC with gas channels, the porous electrodes and dense electrolyte.

The schematic in Fig. 1.1 depicts a SOFC consisting of a dense Yttria-stabilized zirconia (YSZ) electrolyte, a porous nickel/YSZ (Ni/YSZ) anode, and a porous lanthanum strontium manganite/YSZ (LSM/YSZ) cathode. Electrochemical reactions take place at the three-phase boundaries (TPBs) where the pores, ionic phase (YSZ), and electronic phase (Ni/LSM) intersect. At the anode, fuel (H_2) is oxidized to generate protons (H^+) and electrons, which flow through an external circuit to the cathode, producing electric current. At the cathode, O_2 is reduced to O^{2-}, which migrates through the electrolyte to the anode, where it combines with H^+ to form H_2O. To function efficiently, the dense electrolyte requires high ionic conductivity to facilitate the movement of ions while preventing gas crossover, while the anode and cathode must exhibit high catalytic activity, sufficient electronic/ionic conductivity and high gas diffusivity. The development of SOFCs has focused on the development of suitable materials, and new fabrication and characterization techniques have enabled precise calibration of porous materials for optimal architecture design. Numerical simulations also have proven to be a powerful tool in SOFC development and optimization.

Overall, the development of SOFCs has progressed significantly, and the state-of-the-art materials and manufacturing processes have brought the technology closer to commercialization. The ongoing research and development are mainly focused on improving performance, reducing costs, and increasing durability. The following sections provide a brief overview of the current state of SOFC electrode material development and the latest advancements in the field.

Material Development

The benchmark anode material, Ni/YSZ, is a Metal-Fluorites Cermet (see Fig. 1.1) that boasts high electronic/ionic conductivity due to its use of fluorites as electrolyte materials. Additionally, Ni/YSZ exhibits exceptional catalytic properties for carbon-based fuel reforming. However, the material faces several challenges when widely applied:

(i) Hydrocarbon fuels like methane (CH_4) can lead to carbon deposition on the surface of Ni, reducing catalytic properties and obstructing gas transfer through the material's pores.

(ii) Ni is vulnerable to poisoning from various fuel impurities when using biogas or coal gasification, such as sulfur (S), chlorine (Cl), phosphorus (P), arsenic (As), selenium (Se), and antimony (Sb), as well as gases like arsine (AsH_3). These substances can physically or chemically bond with Ni, causing a loss of TPBs and a decline in catalytic performance.

(iii) High temperatures can trigger Ni-particle coarsening, depletion, or migration, leading to microstructure collapse. This destruction impacts TPBs, reduces catalytic surface area, and blocks pores.

(iv) Ni/YSZ delamination can occur, resulting in the loss of TPBs, conductivity reduction, and decreased catalytic activity[14,15,16].

There are specific measures viable to address part of the problems mentioned above. For example, introducing a high steam/carbon (S/C) ratio reduces carbon deposition, but this comes at the cost of low performance. To alleviate poisoning, Ni can be partially replaced with transition metals like copper (Cu), cobalt (Co), or silver (Ag), but this often results in a decrease in catalytic activity[17,18,19]. Alternatively, the Ni/YSZ anode can be modified by incorporating different metals or oxides, such as scandium oxide (Sc_2O_3), ceria (CeO_2), titanium oxide (TiO_2), iron (Fe), molybdenum (Mo), niobium oxide (Nb_2O_5), or alumina (Al_2O_3)[15,20]. Replacing YSZ with ceria (CeO_2)-based electrolyte, such as Gadolinium-Doped Ceria (GDC), Samarium-Doped Ceria (SDC), gadolinium (Gd)- or samarium (Sm)-doped ceria (CGO or CSO), or scandia-stabilized zirconia (ScSZ) has also been explored[21,22]. Studies have shown that CeO_2-based anodes, such as $Ba(Ce_{0.8}Y_{0.1})_{0.8}Ni_{0.2}O_{3-\delta}/Gd_{0.1}Ce_{0.9}O_{1.95}$, perform better than Ni/YSZ in terms of hydrocarbon catalytic properties[23]. However, Ni agglomeration remains a persistent problem.

The use of Ni-free anode materials, such as perovskite (ABO_3)-based mate-

rials, is gaining attention as potential candidates for fuel cell applications. These materials have an A cation larger than the B cation. However, finding a single material that exhibits comparable catalytic activity and ionic/electronic conductivity as Ni/YSZ remains challenging. Perovskite materials usually contain transition metals such as strontium (Sr), niobium (Nb), vanadium (V), titanium (Ti), and others, with variable valence, which is beneficial for mixed conductivity[24,25]. The mixed conductivity is achieved by defects, which can be controlled by doping the host atom with similar-sized cations. For instance, higher oxygen ion conductivity than YSZ is achieved with $(La_{0.9}Sr_{0.1})Ga_{0.8}Mg_{0.2}O_{0.285}$ (LSGM) through A-site doping Sr in lanthanum gallate ($LaGaO_3$)[26]. Lanthanum (La)-doped strontium titanium oxide, $SrTiO_3$ (STO), also exhibits improved ionic conductivity with A-site doping[27].

Titanates and chromites are promising perovskite materials[28,29]. Doping STO with La, Nb, and Y has shown electronic conductivity with stable properties under both oxidizing and reducing conditions[30,31]. However, these components have low ionic conductivity, and Mn and Ga are further introduced into La-doped material with improved ionic conductivity[32]. Perovskites based on V, Co, and Fe, such as $SrVO_3$, $SrFeCo_{0.5}O_x$, $SrCo_{0.8}Fe_{0.2}O_{3-\delta}$, and $La_{0.6}Sr_{0.4}Fe_{0.8}Co_{0.2}O_{3-\delta}$, also show potential for anode materials[33]. $LaCrO_3$, once used as an interconnect material, may also be a possible anode material by doping Mn, Fe, Co, Ni, Ti, and Cu. One such material is $(La_{0.75}Sr_{0.25})Cr_{0.5}Mn_{0.5}O_3$ (LSCM), which has stable conductivity in oxidation and reduction atmospheres[34,35]. Double perovskite ($A_2B_2O_6$)-based materials were also investigated due to reasonable ionic conductivity[36,37,38]. But these materials have low electronic conductivity and catalytic activity. Pyrochlore and tungsten bronze structured compounds were also investigated but with low electronic conductivity and redox stability[39].

For the cathode material, the presence of CO_2, SO_2 and H_2O from the air, Cr from the metallic interconnect, and Si from the glass sealant, which can cause poisoning[40]. Besides, there are also microstructure deformation and delamination problems. Cathode material basically is all perovskite materials such as strontium doped lanthanum manganite perovskite ($La_{1-x}Sr_xMnO_3$) (LSM) with YSZ (LSM/YSZ), strontium doped lanthanum cobalt ferrite ($La_{1-x}Sr_xCo_{1-y}Fe_yO_3$) (LSCF), $Ba_{0.5}Sr_{0.5}Co_{0.8}Fe_{0.2}O_{3-\delta}$ (BSCF), $LnBaCoO5+\delta$ (Ln = Pr, Nd, and Gd) based[41,42,43,44]. Besides, a buffer layer may be applied to decrease impedance and prevent reaction between electrolyte and cathode[45,46].

For both anode and cathode materials, the most commonly used techniques for electrode fabrication are screen printing, dip coating, and extrusion[47]. To optimize the overall performance, the microstructure of the electrodes can be tailored through impregnation/infiltration techniques[48], such as (i) impregnation with metal-salt solutions with various additives, (ii) impregnation with particles in suspension, and (iii) molten salt impregnation. Another promising method to design electrode materials is the exsolution of nano-metal particles in the perovskite material[49,50,51]. In addition, chemical vapour deposition (CVD) and atomic layer deposition (ALD) can be used to fabricate nanoparticles and nano-porous layers in SOFCs[52].

Simulation and Prediction

Simulation has emerged as an essential approach to material and cell development. Simulation can provide detailed information on phenomena that are challenging to measure through experimentation. Depending on the scales involved, different simulation approaches can be used[53]. At the atomic/microscale, Density Functional Theory (DFT)[54], Molecular Dynamics (MD)[55], and Kinetic Monte Carlo (KMC)[56] can be used. At the mesoscale, Lattice Boltzmann Method (LBM), Smoothed Particle Hydrodynamics (SPH) Model, KMC, and Phase Field Model (PFM)[57] are used. On the other hand, Multiphysics Computational Fluid Dynamics (CFD) simulation is used to study the performance of SOFC at the cell scale[58]. Different numerical methods can be applied to simulations, such as Finite Element Method (FEM), Finite Volume Method (FVM), and LBM[59]. Although Multiphysics simulation is at the cell level, the impact of microstructure is also considered for effective diffusion[60], electronic/ionic conductivity[61,62], as well as electrochemical reaction active surface areas[63].

There are numerous studies focused on mesoscale and macroscale simulations. Fu et al.[64] reviewed and proposed a modified model for predicting the long-term performance of SOFCs by considering Ni-particle coarsening. Their study showed that an increase in temperature, current density, steam/carbon ratio, and YSZ particle diameter contributed to an increase in degradation rate. Zhu et al.[65] investigated the impact of Ni-particle coarsening, YSZ structure transition, and interconnect coating on SOFC performance through multiscale numerical simulations. They found an overall degradation rate of 2.2%/1000 h, which could be reduced to 0.43%/1000 h through targeted microstructure design. He et al.[66] developed a numerical model that used a multi-phase level-set approach to optimize the Ni-YSZ anode microstructure, showing that the optimized microstructure and performance were independent of initial structures and

phase division schemes. Bosio and Bianchi developed a multiscale SOFC model that considers degradation arising from Ni-coarsening and Cr poisoning for microstructure and operative condition optimization[67].

The combination of dual-focused ion beam scanning electron microscopy (FIB-SEM) and X-ray computed tomography (X-ray CT) provides a unique opportunity to acquire accurate and real 3D microstructure geometry after fabrication, as discussed in a comprehensive review article by Paul et al.[68]. Utilizing real microstructures obtained by X-ray CT, Matthew et al.[69] developed a modelling framework to gain a better understanding of Multiphysics phenomena. Lu et al.[70] assessed the mass transport properties and electrochemical performance of a hierarchically micro-tube solid oxide fuel cell (SOFC) through an integrated computational fluid dynamics simulation, which was assisted by 3D X-ray CT. Furthermore, Sciazko et al.[71] utilized FIB-SEM in combination with 3D reconstruction to investigate carbon deposition in SOFC anodes and observed a decrease in pore size and volume expansion.

Although, there are numerous research works focused on either material development or numerical simulations. The short lifetime, high cost, and degradation are still problems that hinder the commercialization of SOFCs. In a laboratory environment with low fuel and air utilization, the longest operation known lifetime recorded by Forschungszentrum Jülich GmbH reaches 93,000 hrs, with a degradation rate of 0.5%/1000 h[72]. Bloom Energy has demonstrated hundred kW to MW SOFCs for building power supply, LG Fuel Cell Systems also built a 250 kW SOFC system while Ceres Power demonstrates a 200 MW energy supply for residence application[73]. But there are no SOFCs achieve a degradation rate of less than 0.2 Percent per 1,000 Hours and developing materials with low cost and high performance is still challenging as is highlighted by the US Department of Energy[74].

1.3 Motivation

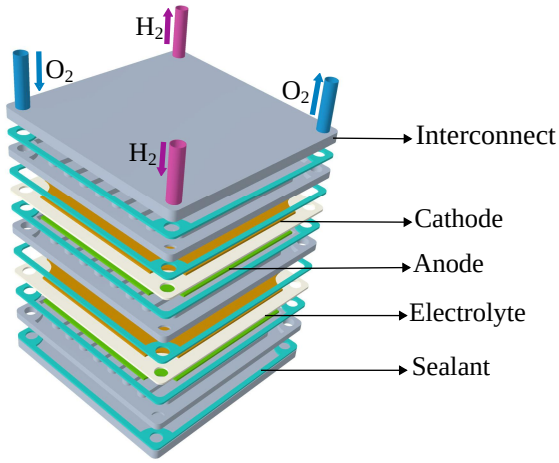

Figure 1.2: Schematic of a SOFC stack of two unit cells with different components (adapted from literature [75]).

Fig. 1.2 [75] shows a SOFC stack comprising of two single SOFCs, each comprising five distinct materials, including the anode, electrolyte, cathode, sealants, and interconnects. The sealant material plays a vital role in gas sealing, preventing leakage during the electrochemical reaction. The interconnect provides support and electronic conductivity. During thermal cycling processes, the coefficient of thermal expansion (CTE) between each material must be matched to avoid mechanical failure. These materials stacked together form four interfaces, and any form of failure in these interfaces can obstruct power output or lead to performance degradation [76].

Apart from the problems mentioned for electrode materials, there are issues such as phase transition in the electrolyte [77], interconnect corrosion [78], and structural issues with sealant materials [79]. However, most critical degradation issues are related to TPB at the porous electrode which extends for dozens of micrometres from the dense electrolyte as is stressed in the previous section [80]. The degradation in a porous electrode is always accompanied by changes in the microstructure, which can reduce gas transport, charge transport, and electrochemical catalytic properties [81]. Generally, the following criteria must be satisfied for active electrodes: (i) high electronic ionic conductivity; (ii) high catalytic activity; (iii) redox stability; (iv) chemical stability; (v) thermal stability; (vi) CTE matching.

Optimising the microstructure of porous electrodes provides a way to avoid or mitigate the problems mentioned above. To optimise the microstructure architecture of SOFC electrodes, quantitatively characterising the properties is essential. However, there are no standard approaches for microstructure evaluation for the porous electrode. The accuracy of different approaches is questionable. Therefore, it is necessary to compare the differences between different approaches. The microstructure parameters can be applied to multiscale and Multiphysics coupled simulations. Simulation of SOFC must consider the electrochemical reactions and gas diffusion which determine the performance. There exist different models in the literature for the simulation of these processes. Different models behave differently in SOFC simulation. Knowledge of the differences between these models is essential for accurate SOFC model development. The Multiphysics model developed takes the microstructure parameters into consideration and can be used to assist electrode and cell optimization design within different scales. Therefore, the following objectives are proposed.

1.4 Objectives

Based on advanced tomography techniques, the parameters related to gas transport in a porous electrode are obtained. The microstructure data with CFD Multiphysics simulation of SOFC provide a more understanding of the performance across multiple scales. The models then can be used to optimise either single-cell or stacks regarding electrochemical and mechanical performances. Therefore, the thesis aims to conduct experiments with advanced tools and techniques to investigate the microstructure parameters and their relationship with electrochemical performance. Followed by developing Multiphysics models for parametric optimizations and thermal stress simulations. The following work then was conducted:

- A button SOFC with two anode compositions is prepared and tested using an electrochemical workstation. After testing, FIB-SEM is used to characterize the SOFC and get the 2D slice images. Based on 2D slice images, the 3D microstructure of the porous anode is constructed. Different approaches are compared to calculate tortuosity.
- Fully coupled Multiphysics 3D SOFC model is constructed. To develop and optimize the model, different electrode kinetics models and different diffusion models are examined and compared.

- On the basis of the optimized Multiphysics model, the tortuosity and electrode composition impact on SOFC performance are investigated.
- Thermal stress distribution of a button SOFC is analysed using different sealant materials. In addition, thermal stress at the micro-scale is also simulated based on a micro SOFC model.

1.5 Thesis outline

The thesis is organized into five chapters. Chapter 1 provides an introduction to the background, state of art, motivation, and objectives of the thesis. Chapter 2 provides a fuel cell basics which includes its history and the theory behind it, from thermodynamics to electrochemical reaction kinetics. Chapter 3 introduces the governing equations for SOFC simulations. Chapter 4 focuses on the experimental procedures and methods used for tortuosity calculations. Chapter 5 presents the results of the research, including the impact of different electrochemical kinetics, microstructure, and tortuosity on SOFC performance. Additionally, thermal stress is analyzed based on a button SOFC model and a micro SOFC model. Finally, Chapter 6 offers conclusions and future outlooks for SOFC research. The related papers are appended at the end of the thesis, providing readers with further insights into the research and methods employed. Overall, the thesis provides a comprehensive analysis of SOFCs and lays the foundation for future research in the field of sustainable energy systems.

Chapter 2

Fuel cell explained

2.1 History and principle of fuel cells

The concept of SOFCs can be traced back to the 18th century when the discovery of water electrolysis was first made[82,83]. After that, the principle of FC was independently published by Friedrich Schönbein (1799-1869) and Welsh scientist William Robert Grove (1811-1896). However, it is until the discovery of ionic and electronic conductors that scientists start looking for a suitable electrolyte for fuel cells[84,85]. Later on, the term cathode, anode, and positive/negative electrode are coined by Faraday.

To understand the principle of fuel cells and develop various types of fuel cells, scientists have made significant discoveries in electrochemistry science since 1838. The discoveries of electronic and ionic conduction, combined with the application of thermodynamics, have led to the development of different types of fuel cells with various electrolytes. These types include polymer electrolyte fuel cells (PEMFCs), alkaline fuel cells (AFCs), phosphoric acid fuel cells (PAFCs), molten carbonate fuel cells (MCFCs), and solid oxide fuel cells (SOFs). Each type has its own advantages and disadvantages, and the appropriate type should be chosen depending on the specific application and operating conditions.

The SOFC use a solid electrolyte which is sandwiched between the porous anode and porous cathode as is depicted in Fig. 1.1. Based on different criteria, SOFCs can be classified by geometry (planar, tubular, flat tube, monolithic), support type (electrolyte support, anode support, cathode support), fuel type (direct alcohol SOFC, direct carbon SOFC), and

chamber type (double, single, or without chamber)[86]. For planar SOFCs, it is scaled up by stacking individual cells in series to form stacks. Additional components such as sealants and interconnects are required for sealing and electrical connection[87,88]. In order to achieve optimal efficiency, external auxiliary equipment such as gas storage and regulator systems, pre-reformers, exhaust gas treatment, and heat treatment is necessary[89].

2.2 Thermodynamics

To understand the energy conversion process in a SOFC, it is useful to consider it as a thermodynamic system, characterized by various intensive and extensive properties at equilibrium. Combined the first law of thermodynamics and the second law of thermodynamics we can get the Gibbs equation[90]:

$$\Delta G = \Delta H - T \cdot \Delta S. \tag{2.1}$$

where ΔG is the available electricity work, ΔH is the enthalpy change of the chemical reaction, and ΔS is the entropy change of the system.

For fuel cell operating reversibly with pure H_2 and O_2, the maximum ideal electrical efficiency at standard ambient temperature and pressure (SATP)[1] is 83% (1.23 V) when $\Delta S > 0$. However, this efficiency decreases to 62% (0.92 V) at 1000 $°C$, 1 atm in the case of SOFC[91]. On the other hand, the thermodynamic efficiency for direct carbon fuel cells (DCFCs) can exceed 100% by absorbing energy from the surroundings since $\Delta S < 0$[92]. The actual efficiency of a fuel cell system is influenced by internal losses and the support system, such as gas composition, overpotential, and work loss. Nevertheless, fuel cell systems can be optimized to achieve high efficiency, with more than 60% electricity efficiency and even higher when combined with a gas turbine, heating, and cooling system[93,94].

The electrical voltage for fuel cell utilizing H_2 can be related to thermodynamic quantity by power[95]:

$$P = E^0 \cdot I = \dot{n}_{H_2} \cdot \Delta G^0. \tag{2.2}$$

where the current I is expressed as spent of fuel, $-2\dot{n}_{H_2} \cdot F$, then the reversible voltage, also known as the standard cell potential, can be expressed as:

[1] Pure gas at a temperature of 298.15 K and an absolute pressure of 1 atm.

$$E^0 = -\frac{\Delta G^0}{n \cdot F}. \tag{2.3}$$

By considering species impact on the cell voltage, assume ideal gas, the Gibbs energy can be expressed as:

$$\Delta G = \Delta G^0 + RT \ln Q. \tag{2.4}$$

The Nernst equation determine the open circuit voltage E^{OCV} then can be expressed as:

$$E^{OCV} = -\frac{\Delta G^0 + RT \ln Q}{n \cdot F} = E^0 - \frac{RT \ln Q}{n \cdot F}, \tag{2.5}$$

where Q is the reaction quotient and the open circuit voltage $E^{OCV}_{H_2/O_2}$ for fuel cell fueled with H_2 can be written as[96,97]:

$$E^{OCV}_{H_2/O_2} = E^0 - \frac{RT}{2F} \ln \frac{p_{H_2O,TPB}}{p_{H_2,TPB} p^{0.5}_{O_2,TPB}}. \tag{2.6}$$

The standard cell potential (E^0), expressed as the standard reaction Gibbs energy difference ΔG^0, is related to the temperature by using the thermodynamic properties of the reaction at SATP conditions. For the SOFC with H_2 as fuel, the enthalpy ΔH^0 is -241.79 kJ/mol and the entropy ΔS^0 is -47.30 J/mol/K. Based on these value, the standard cell potential (E^0) can be expressed as follows[98,99,100,101]:

$$E^0 = 1.253 - 2.4516 \times 10^{-4} T. \tag{2.7}$$

It is noted that the partial pressure of species i is $p_i = x_i p_{a/c}$. This leads to the Nernst equation, Eq. (2.6) expressed as[102]:

$$E^{OCV}_{H_2/O_2} = E^0 - \frac{RT}{2F} \ln \frac{x_{H_2O,TPB}}{x_{H_2,TPB} x^{0.5}_{O_2,TPB}} + \frac{1}{2} \ln p_c. \tag{2.8}$$

The pressure, partial pressure, and molarity can be extracted from the electrode, i.e. TPB. The equilibrium voltage can be divided into two components: anode side $E^{OCV}_{H_2}$ and cathode side $E^{OCV}_{O_2}$[103].

$$\begin{cases} E^{OCV}_{H_2} = E^0 - \frac{RT}{2F} \ln \frac{p_{H_2O,TPB}}{p_{H2,TPB}}, \\ E^{OCV}_{O_2} = -\frac{RT}{2F} \ln \frac{1}{p^{0.5}_{O2,TPB}}, \\ E^{OCV}_{H_2/O_2} = E^{OCV}_c + E^{OCV}_a. \end{cases} \tag{2.9}$$

2.3 Electrochemical kinetics

Thermodynamics has revealed the electrochemical force (potentials) at a given electrode state where electrochemical reactions can occur. However, it doesn't provide information about whether the reaction will proceed or at what rate it will occur. This will be explained by electrochemical kinetics, which is the topic of interest in **Paper II**. The rate of electrochemical reaction is proportional to the current flow through the electrode. When current flows through the electrode, polarization or voltage loss occurs. Essentially, all rate processes during current flow, including reaction and transport processes, require driving forces (potential energy) to proceed, leading to ohmic polarization (η_{ohm}), concentration polarization (η_{conc}), and activation polarization (η_{act}). As a result, the actual cell voltage E is lower than the open circuit voltage[104,105].

$$E = E^{OCV}_{H_2/O_2} - \eta_{ohm} - \eta_{conc} - \eta_{act}. \tag{2.10}$$

Ohmic polarization is caused by the ionic resistance in the electrolyte and active electrode; electronic resistance in the electrode, current collector, and interconnect. In most cases, the contact resistance can be neglected due to good contact between the SOFC components. The ohmic polarization can be expressed as[106]:

$$\eta_{ohm} = i(R_s + R_l). \tag{2.11}$$

At high current densities, concentration polarization becomes dominant, and it can be described as[106]:

$$\eta_{conc} = \frac{RT}{nF} \ln \frac{p_{H_2O,TPB} p_{H_2,b}}{p_{H_2,TPB} p_{H_2O,b}} + \frac{RT}{nF} \ln \frac{p^{0.5}_{O_2,b}}{p^{0.5}_{O_2,TPB}}. \tag{2.12}$$

The right-hand side of the equation consists of two terms: the concentration polarization in the anode ($\eta_{conc,a}$) and the concentration polarization in the cathode ($\eta_{conc,c}$).

The activation polarization is caused by the activation energy required to initiate the electrochemical reaction. It can be expressed as follows for the anode and cathode, which can be further correlated with current density[102,107]:

$$\begin{cases} \eta_{act,a} = \phi_{s,a} - \phi_{l,a} - E^{OCV}_{H_2}, \\ \eta_{act,c} = \phi_{s,c} - \phi_{l,c} - E^{OCV}_{O_2}, \end{cases} \tag{2.13}$$

where $\phi_{s,a/c}$ are the electronic potential in anode (a) and cathode (c), while $\phi_{l,a/c}$ are the ionic potential in anode and cathode.

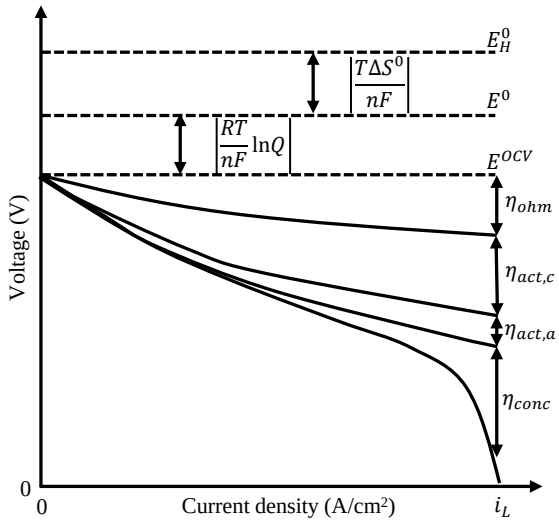

Figure 2.1: Description of a typical fuel cell polarisation curve showing the original standard enthalpy ΔH^0 converted voltage E_0^H, standard Gibbs free energy ΔG^0 converted voltage E_0 (equilibrium state) and open circuit voltage E^{OCV}. The operation voltage E deviate from the open circuit voltage due to various polarisation.

Figure 2.1 displays the polarization curve of a typical unit SOFC, showing the deviation of the operation voltage E from the open circuit voltage E^{OCV} due to various polarizations in the anode and cathode[108]. The theoretical potential is $E_H^0 = \Delta H^0/(nF)$ when the entropy change ΔS_0 equals 0, while $E^0 = \Delta G^0/(nF)$ is the standard cell potential considering entropy loss. For SOFCs operated at high temperatures, compared to low-temperature PEMFCs, the difference between E^0 and E^{OCV} is smaller. At low current densities, energy is required to overcome the reaction barrier, resulting in the dominance of activation polarization η_{act}. As the current density increases, the ohmic polarization becomes more significant. At very high current densities, the gas species cannot be supplied fast enough, leading to the dominance of concentration polarization. Notably, all of these polarizations coexist throughout the operation stages.

The rate of electron transfer, which is related to the current density i, is also affected by activation polarization and species concentration depending on specific working conditions. When the electrochemical reaction is at an equilibrium state, the forward and backward reaction rates are the same, which means that the anodic current density (i_a) and cathodic current

density (i_c) is equal to the exchange current density (i_0). The general Butler-Volmer (BV) equation can be expressed as:

$$i = i_0 \left[\exp\left(\frac{n\alpha F\eta}{RT}\right) - \exp\left(\frac{-n(1-\alpha)F\eta}{RT}\right) \right]. \tag{2.14}$$

The overall current density, related to the overpotential η, Eq. 2.14 is also called the activation-controlled Butler-Volmer equation, which only considers the activation polarization impact on current density [109]. There is also a diffusion-controlled BV equation which considers the species concentration impact on current density [106]:

$$i = i_0 \left[\frac{x_{O,TPB}}{x_{O,b}} \exp\left(\frac{n\alpha F\eta}{RT}\right) - \frac{x_{R,TPB}}{x_{R,b}} \exp\left(\frac{-n(1-\alpha)F\eta}{RT}\right) \right]. \tag{2.15}$$

It is noted that both types of BV equation use the exchange current density as follows:

$$i_{0,a/c} = \frac{RT}{nF} k_{a/c} \exp\left(-\frac{E_{a/c}}{RT}\right). \tag{2.16}$$

In the equation above, k represents the pre-exponential factor of the exchange current density for the electrode reaction, while $E_{a/c}$ is the activation energy for the electrode. For a given reaction, the reactants and products occupy energy minima for stability. In a forward reaction, the potential energy of the reactants must first rise, then fall to reach the minimum energy and form products. The difference in energy between the maximum and the reactants is the activation energy for the forward reaction. For Ni/YSZ anodes, the activation energy range is 50-189 kJ/mol, while for LSM-YSZ cathodes, it is 70-293 kJ/mol. These values are summarized in **Paper II**.

The comparison of simulation results for the activation-controlled and diffusion-controlled BV equation for SOFCs is presented in **Paper II**. Notably, the current density for both equations is a surface value with units of [A/cm^2]. The anode and cathode's active layer typically consists of a mix of ionic and electronic conductors, extending the electrochemical reaction to a depth of 20-40 μm. Examples of such material for SOFC anodes and cathodes include Ni/YSZ and LSM/YSZ as mentioned before [110]. To relate the TPB to the electrochemical rate, defining an active surface area per unit volume is necessary, typically denoted as the area-to-volume ratio a_v [m^2/m^3]. This parameter can be used in the BV equation to obtain the volumetric current density i_v. Various literature sources report active specific area values for SOFC anodes and cathodes, which can be found in

Paper II. It is noted that replacing exchange current density (2.16) in BV Eq.(2.14) with the exchange current density as follow is also used[111,112]:

$$i_{0,c} = k_c \left(\frac{p_{O_2}}{p_{O_{2,ref}}} \right)^C \exp\left(-\frac{E_c}{RT} \right), \tag{2.17}$$

$$i_{0,a} = k_a \left(\frac{p_{H_2}}{p_{H_{2,ref}}} \right)^A \left(\frac{p_{H_2O}}{p_{H_2O_{2,ref}}} \right)^B \exp\left(-\frac{E_a}{RT} \right). \tag{2.18}$$

where $k_{a/c}$ is the pre-exponential factor which is different from Eq.(2.16), and A, B, and C are obtained from experiments.

Chapter 3

Governing equations

3.1 Charge transport

The OCV of a cell is determined by the Nernst equation, as shown in Eq. (2.5). The cell voltage accounts for the losses due to activation, ohmic, and concentration overpotential, as expressed in Eq. (2.10). The activation overpotential η_{act} is explicitly related to the current density i through the BV equation, as shown in Eq. (2.15). The concentration of species is also included in the BV equation through the exchange current density i_0, as shown in Eqs. (2.17) and (2.18), resulting in an implicit inclusion of concentration. An additional expression for concentration overpotential is defined in Eq. (2.12). The ohmic overpotential loss is also implicitly included through Ohm's Law, which describes the flux of charges (ions/electrons) in a homogeneous electrode or electrolyte:

$$i_s = -\sigma_s^{eff} \nabla \phi_s. \tag{3.1}$$

$$i_l = -\sigma_l^{eff} \nabla \phi_l, \tag{3.2}$$

Here, σ_s^{eff} and σ_l^{eff} represent the effective electronic and ionic conductivity, respectively, while ϕ_s and ϕ_l represent the electronic and ionic potential, respectively. It is reasonable to conclude that the ionic conductivity is for O^{2-} transport, while the electronic conductivity is for e^- transport. The same applies to the electronic and ionic potentials, which are the potentials felt by electrons and ions, respectively. The ionic and electronic conductivity can be expressed as follows[113]:

$$\sigma_l = 33.4 \times 10^3 \exp\left(\frac{-10300}{T}\right). \tag{3.3}$$

$$\sigma_{s,c} = \frac{4.2 \times 10^7}{T} \exp\left(\frac{1200}{T}\right). \tag{3.4}$$

$$\sigma_{s,a} = \frac{9.5 \times 10^7}{T} \exp\left(\frac{-1150}{T}\right). \tag{3.5}$$

The actual conductivity of the electrode is lower than the pure ionic and electronic bulk due to the porous nature of the electrode. Therefore, the effective ionic and electronic conductivity in the active anode and cathode needs to be corrected by the tortuosity (τ), which will be introduced later[114].

$$\sigma_{l,a/c}^{eff} = \sigma_{l,a/c} \frac{V_{l,a/c}}{\tau_{l,a/c}}. \tag{3.6}$$

$$\sigma_{s,a/c}^{eff} = \sigma_{s,a/c} \frac{V_{s,a/c}}{\tau_{s,a/c}}. \tag{3.7}$$

The Nernst-Planck equation is a conservation of mass equation that is commonly used to describe the transport of charged species due to diffusion, convection, and electromigration. However, for solid oxide fuel cells (SOFCs), only electromigration is considered[115].

$$\nabla \cdot i_l = \begin{cases} i_v & \text{in the active air electrode,} \\ 0 & \text{in other solid components,} \\ i_v & \text{in the active fuel electrode,} \end{cases} \tag{3.8}$$

$$\nabla \cdot i_s = \begin{cases} -i_v & \text{in the active air electrode,} \\ 0 & \text{in other solid components,} \\ -i_v & \text{in the active fuel electrode,} \end{cases} \tag{3.9}$$

The current source term i_v is given by the BV equation as $a_v i$ described in Chapter 2.

3.2 Momentum transport

The governing equations for multiphysics SOFC simulation are in a steady-state regime. The fluid flow in SOFC can be assumed either incompressible or compressible. When assuming incompressible flow, the divergence of density (ρ_f) is zero, and it is a function of temperature (T) and constant pressure (p). The fluid is assumed to be a Newtonian fluid with a linear relationship between stress and strain. Moreover, there is no source term in

the gas channel, and the gravity term is neglected. Therefore, the continuity and momentum in the gas channel can be expressed as:

$$\nabla \cdot (\rho_f \mathbf{u}) = 0, \tag{3.10}$$

$$\rho_f(\mathbf{u} \cdot \nabla)\mathbf{u} = \nabla \cdot [-p\mathbf{I} + \mu_f(\nabla \mathbf{u} + (\nabla \mathbf{u})^T)], \tag{3.11}$$

where $\mathbf{u}$ is the velocity vector, $\mathbf{I}$ is the identity matrix, and μ_f is the dynamic viscosity of the fluid mixture, which depend on the thermodynamic state of the gas species as will be discussed in section 3.3.

When considering fluid flow in a porous medium, it is often impractical to fully resolve the flow through the porous structure due to the complexity of the solid wall. Thus, a common approach is to treat the porous medium as homogeneous. Darcy's Law describes the linear relationship between the velocity field $\mathbf{u}$ and the gradient of pressure p in a porous material with fully saturated flow:

$$\mathbf{u} = -\frac{\kappa}{\mu_f}\nabla p, \tag{3.12}$$

where κ is the permeability of the porous medium. Darcy's law, together with the continuity equation (Eq. (3.10)) and the equation of state, describes fluid flow at very low velocities or low Reynolds numbers ($\mathrm{Re} < 10$), where the impact of shear stress on the flow can be ignored. A nonlinear relationship between velocity and pressure gradient is also available, which can be obtained by introducing additional terms based on Eq. (3.12) or by using a different permeability model. To account for the shear stress in porous medium flow, the Brinkman equations should be used[116].

$$\nabla \cdot (\rho_f \mathbf{u}) = Q_m, \tag{3.13}$$

$$\frac{1}{\varepsilon}\rho_f \left(\mathbf{u} \cdot \nabla\right) \mathbf{u}\frac{1}{\varepsilon} = -\nabla \cdot (-p\mathbf{I} + \mathbf{K}) - \left(\kappa^{-1}\mu_f + \beta\rho_f \mathbf{u}\left|\mathbf{u}\right| + \frac{Q_m}{\varepsilon^2}\right)\mathbf{u}, \tag{3.14}$$

The dependent variables in this equation are Darcy's velocity $\mathbf{u}$ (superficial volume average) and pressure p. Here, β represents the Forchheimer coefficient, ε is the porosity, and Q_m is the mass source or sink of the reaction m, which is only present in the active electrode where the electrochemical reaction takes place. The density is obtained from the equation of state, and the gravitational force term is neglected.

The Brinkman equations account for the dissipation of kinetic energy due to viscous shear, similar to the Navier-Stokes equations. The viscous stress tensor $\mathbf{K}$ is given by[116]:

$$\mathbf{K} = \mu_f \frac{1}{\varepsilon}\left(\nabla \mathbf{u} + (\nabla \mathbf{u})^T\right) - \frac{2}{3}\mu_f \frac{1}{\varepsilon}\left(\nabla \cdot \mathbf{u}\right)\mathbf{I}. \tag{3.15}$$

The viscous tensor includes stresses related to linear deformation and volumetric deformation, corresponding to the first and second terms on the right-hand side.

3.3 Mass transport

The mass transport of an individual species in the gas channel can be calculated as follows:

$$\rho_f \left(\mathbf{u} \cdot \nabla\right) \omega_i = -\nabla \cdot \mathbf{j}_i + R_i, \tag{3.16}$$

where ω_i is the mass fraction of gas component i, R_i is the mass source or sink, which appears in the active electrodes, and $\mathbf{j}_i$ is the mass flux term. In the anode support layer, the mass source or sink term R_i only appears when there are internal reforming reactions such as water gas shift reaction (WGSR) and methane-steam reforming (MSR) reactions [117]. According to the continuity equation Eq. (3.10):

$$\sum_{i=1}^{N} \omega_i = 1; \quad \sum_{i=1}^{N} \mathbf{j}_i = 0; \quad \sum_{i=1}^{N} R_i = 0, \tag{3.17}$$

where M and M_i are the mean molar mass and the molar mass of species i. The density ρ_f according to ideal gas law can be written as:

$$\rho_f = \frac{pM}{RT}. \tag{3.18}$$

The mass fraction ω_i and molar fraction x_i is defined as:

$$\frac{1}{M} = \sum_{i=1}^{N} \frac{\omega_i}{M_i}; \quad x_k = \frac{\omega_k}{M_k} M, \tag{3.19}$$

The flux of species i can be expressed according to the Maxwell-Stefan description (Fick equation) [118]:

$$\mathbf{j}_i = -\rho \omega_i \sum_{k=1}^{N} \tilde{D}_{ik} \mathbf{d}_k, \tag{3.20}$$

$$\frac{x_i x_k}{D_{ik}} = -\omega_i \omega_k \frac{\sum_{j \neq i} \left(\mathrm{adj} B_i\right)_{jk}}{\sum_{j \neq i} \tilde{D}_{ij} \left(\mathrm{adj} B_i\right)_{jk}}, \quad (B)_{kj} = \tilde{D}_{kj} - \tilde{D}_{ij}, \quad i \neq j, \tag{3.21}$$

$$\mathbf{d}_k = \frac{1}{cR_gT}\left(\nabla p_k - \omega_k \nabla p\right). \tag{3.22}$$

The multicomponent Fick diffusivities are denoted by $\tilde{D}ik$, which are symmetric, i.e., $\tilde{D}ik = \tilde{D}ki$, and the Maxwell-Stefan diffusion coefficient is denoted by Dik, which is also symmetric. The adjoint matrix B_i has jk^{th} component $\left(\mathrm{adj}B_i\right)_{jk}$. The diffusion driving force acting on species k is denoted by $\mathbf{d}_k$. The driving force $\mathbf{d}_k$ is related to the gas constant R_g, total molar concentration c, and pressure p of all species. The partial pressure and mass fraction of species k are denoted by p_k and ω_k, respectively. It is important to note that the diffusion flux due to thermal gradient is ignored, i.e., the diffusion force does not affect heat transfer. Furthermore, external forces such as gravity and electromotive force are ignored in the driving force. By applying the ideal gas law and using $p_k = x_k p$, the driving force $\mathbf{d}_k$ can be expressed as:

$$\mathbf{d}_k = \nabla x_k + \frac{1}{p}\left[\left(x_k - w_k\right)\nabla p\right], \tag{3.23}$$

where $x_{i/k}$, $M_{i/k}$ is the molar fraction and molar weight of the specie i or k. The gas species diffuse freely in the gas channel, where the interaction between gas molecules is dominant. According to Chapman and Enskog, the binary gas diffusion coefficient at low pressure predicted from the theory can be written as[119]:

$$D_{ik} = \frac{3}{16}\frac{\left(4\pi k_B T/M_{ik}\right)^{1/2}}{n\pi\sigma_{ik}^2\Omega_D} f_D, \tag{3.24}$$

$$M_{ik} = \frac{2}{\frac{1}{M_i} + \frac{1}{M_k}}, \tag{3.25}$$

where M_i and M_k is the molecular weight of i and$k$, n, k_B, T are the number density of molecules in the mixture, Boltzmann constant and absolute temperature. The collision integral Ω_D for diffusion is a function of temperature, and the characteristic length σ_{ij} depends on the selected intermolecular force law. If M_i is of the same order as M_k, the correction term f_D is between 1.0 and 1.02, then replace n with the ideal gas law we get the binary diffusion coefficient:

$$D_{ik} = \frac{2.66 \cdot 10^{-8} T^{3/2}}{p M_{ik}^{1/2} \sigma_{ik}^2 \Omega_D}. \tag{3.26}$$

The empirical correlation developed by Fuller et al. also is used to describe the diffusion in SOFC[120]. Then the multicomponent Fick diffusivities can

be expressed as:

$$\frac{x_i x_k}{D_{ik}} = -\omega_i \omega_k \frac{\sum_{j \neq i} (adj(B_i)_{jk})}{\sum_{j \neq i} \tilde{D}_{ik} (adj(B_i)_{jk})}, \text{with } (B_i)_{jk} = \tilde{D}_{jk} - \tilde{D}_{ij}, \quad (3.27)$$

while in the porous material, the diffusion coefficient D_{ik} is corrected by porosity ε and tortuosity τ:

$$D_{ik}^{eff} = \frac{\varepsilon}{\tau} D_{ik}, \quad (3.28)$$

where D_{ik} can be either the diffusivity expressed as Eq. 3.26 or Fuller Schettler Giddings model[121]. When species diffuse in a porous electrode, there will be an interaction between the molecule and the solid walls, when the mean free path of the gas species is equal to or larger than the pore size. The diffusion under such conditions is called the Knudsen diffusion. Normally, both molecule diffusion and Knudsen diffusion should be considered and meanwhile, the microstructure must be considered[122,123,124]:

$$D_{ik}^{eff} = \frac{\varepsilon}{\tau} \frac{D_{ik} D_{K,ik}}{D_{ik} + D_{K,ik}}, \quad (3.29)$$

$$D_{K,ik} = \frac{2}{3} r_e \sqrt{\frac{8RT}{\pi M_{ik}}}, \quad (3.30)$$

where ε, τ and r_e are the porosity, tortuosity, and effective pore radius. The detailed introduction to τ will be presented in chapter 4. Todd and Young summarized the thermodynamics and transport properties of the gas and mixture[125]. The dynamic viscosity for individual species and fluid mixture can be expressed as follows:

$$\mu_i = \sum_{k=1}^{7} b_k \left(\frac{T}{1000} \right)^k, \quad (3.31)$$

$$\mu_f = \sum_{i=1}^{N} x_i \mu_i, \quad (3.32)$$

where b_i is the species-dependent parameter.

3.4 Heat transfer

Since SOFCs operate at high temperatures, it is crucial to analyze heat transfer and temperature distribution to prevent cracks and failure caused

by large temperature gradients. The radiation between surfaces and interactions with the media are neglected. Heat transfer in the solid components (i.e., electrolyte and interconnect) can be modelled:

$$\nabla \left(-k_s \nabla T\right) = Q, \tag{3.33}$$

where k_s is the thermal conductivity of the solid, and Q is the heat source due to resistance loss in the electrolyte and interconnects, respectively. By neglecting radiation flux, pressure work, and viscous dissipation, the heat transfer in the gas channel can be written as follows:

$$\rho_f C_{p,f} \mathbf{u} \cdot \nabla T + \nabla \left(-k_f \nabla T\right) = 0, \tag{3.34}$$

where $C_{p,f}$, k_f are the specific heat capacity under constant pressure and the thermal conductivity of the fluid. The first and second terms on the left-hand side are heat transfer as a result of convection and conduction, respectively. However, for porous material, there are local temperature equilibrium hypotheses (LTE) and local temperature no-equilibrium (LTNE) hypotheses[126,127]. By assuming LTE, both the solid and the fluid phases have the same temperature, and the governing equation takes the same form as in the channel[128].

$$\rho_f C_{p,f} \mathbf{u}_{eff} \cdot \nabla T + \nabla \left(-k_{eff} \nabla T\right) = Q, \tag{3.35}$$

where the effective velocity $\mathbf{u}_{eff}$ equals to $\mathbf{u}/\varepsilon$. Depending on heat transfer between the solid and pores, different effective heat conductivity can be used. Parallel heat conduction assumes the effective thermal conductivity k_{eff} expressed as $\varepsilon k_f + k_s/(1-\varepsilon)$, with $k_{s,f}$ the thermal conductivity of solid and fluid. The heat capacity at constant pressure $C_{p,s}$ for individual species and fluid mixture can be written as[125]:

$$C_{p,i} = \frac{\sum_{k=1}^{7} a_k \left(\frac{T}{1000}\right)^k}{M_i}, \tag{3.36}$$

$$C_{p,f} = \sum_{i=1}^{N} \omega_i C_{p,i}, \tag{3.37}$$

where a_k is the species-dependent parameter. The thermal conductivity for individual species and fluid mixture is calculated as[125]:

$$k_i = 0.01 \sum_{k=1}^{7} c_k \left(\frac{T}{1000}\right)^k, \tag{3.38}$$

$$k_f = \sum_{i=1}^{N} x_i k_i, \tag{3.39}$$

where c_k is the species-dependent parameter.

3.5 Source terms

The current source term is governed by the BV equation as shown in Eq. (2.14) and (2.15). The BV equation is also divided into active-controlled BV equation and diffusion-controlled BV equation which will be described in Chapter 5. Besides, the Tafel equation is also a commonly used electrochemical reaction kinetics model, which assumed the rate-limiting steps are the electron and ions transfers, i.e., very small current densities.

3.5.1 Mass and momentum sources

In the porous electrode, where the electrochemical reaction occurs, there is a mass source term. It should be noted that when CH_4 or CO is used as fuel, methane steam reforming (MSR) and water gas shift reaction (WGSR) occur in the porous anode, which results in extra source terms for mass, momentum and heat transfer equations. The volumetric source term in Eq. (3.13) and (**??**) is due to electrochemical reactions in the active porous material, while in the gas channel and support layer, it is zero. The mass source or sink for species i according to Faraday's law can be written as:

$$R_i = -M_i \frac{\nu_i i_v}{nF}. \tag{3.40}$$

The total mass source in the momentum equation (Eq. (3.14)) is determined as:

$$Q_m = -\sum_{i=1}^{N} M_i \frac{\nu_i i_v}{nF}, \tag{3.41}$$

where ν_i is the stoichiometric coefficient for the half-cell reaction in the reduction form, while for the oxidant it is negative and positive for the reductant. The Eq. (3.16) itself is a nonconservative form regarding the convection term with which the source term should be:

$$R_{i,nonconservative} = R_i - \omega_i \sum_{i=1}^{N} R_i. \tag{3.42}$$

3.5.2 Heat sources

There are reversible and irreversible heat sources in a SOFC. The reversible heat source is caused by the polarization loss resulting from the ohmic

resistance and polarization resistance.

$$Q_J = -\left(i_{el} \cdot \nabla\phi_{el} + i_{ion} \cdot \nabla\phi_{ion}\right), \tag{3.43}$$

$$Q_{pol} = \left(\eta_{con} + \eta_{act}\right) i_v, \tag{3.44}$$

$$Q_{rev} = \frac{T\Delta S_r}{n_{el}F}, \tag{3.45}$$

where Q_J is the joule heating due to the ohmic polarization, Q_{pol} is the heat generated by concentration and activation polarization, Q_{rev} is the reversible heat source of the reversible electrode reaction with ΔS_r is the entropy change.

3.5.3 Boundary conditions

The inlet mole fraction for the fuel is 0.9:0.1 (H_2:H_2O), and the air is 0.21:0.79 (O_2:N_2). For outlet, the diffusion term is forced to be zero, i.e., gas is only flowing out by convection. While the normal flux is equal to zero on the wall. For momentum, the inlet is a velocity boundary which assumes fully developed flow, and the outlet is a pressure boundary. The rest of the walls are set in the no-slip condition. For temperature, the inlet is Dirichlet boundary condition and the heat conduction is zero at the outlet and walls. In most cases, the electronic potential ϕ_s on the interconnect surface is assigned as the working potential (0.7 V) on the cathode side and zero on the anode side for SOFC, using a Dirichlet boundary condition. All other boundaries are typically set to an isolation condition, where the flux of electrons and ions across the boundary is zero, i.e., $-\mathbf{n} \cdot i_{el,ion} = 0$. For solid mechanics, there are fixed boundary conditions and free boundary conditions. The detailed boundary conditions are list in the table below.

Table 3.1: Boundary conditions for different physical interfaces.

Settings	Mass	Momentum	Heat	Electric	Mechanics
Inlet	$\omega_i = \frac{x_{0,i}M_i}{M_n}$	Fully flow	$T = T_0$	$\phi_s = \phi_{s,bnd}$	
Outlet	$-\mathbf{n} \cdot \rho\omega_i \sum_k \tilde{D}_{i,k}\mathbf{d}_k = 0$	Pressure	$-\mathbf{n} \cdot \mathbf{q} = 0$	$\phi_s = 0$	Fixed/Free
Walls	$\mathbf{n} \cdot \mathbf{j} = 0$	$\mathbf{u} = 0/\mathbf{u}_{tr}$	$-\mathbf{n} \cdot \mathbf{q} = 0$	$-\mathbf{n} \cdot \mathbf{i}_{l,s} = 0$	

Chapter 4

Experiment procedural and tortuosity calculation methods

4.1 Experiment

4.1.1 Preparing SOFC

In the previous chapter, we delved into the intricate components that make up a solid oxide fuel cell (SOFC). Specifically, we learned that a unit SOFC consists of three essential elements: a dense electrolyte, a porous anode, and a cathode. The electrolyte is responsible for facilitating ion transfer, while the anode and cathode support electrochemical reactions. Moreover, the anode and cathode also function as transport media for gas and charge species. To create a fully operational SOFC system, the individual SOFC units must be connected and sealed using interconnects and sealants. However, depending on the fuel source, the external fuel preparation, air supply, thermal management, water management, and electrical power conditioning equipment may also be necessary[98]. It's worth noting that the development of electrode material plays a crucial role in the advancement of SOFC technology.

Historically, metals were utilized as anode and cathode materials in solid oxide fuel cells (SOFCs) owing to their catalytic activity in the oxidation and reduction reactions[75]. However, this approach had a major drawback as

metals have a CTE that is not compatible with the adjacent electrolyte material, typically Y_2O_3 stabilized ZrO_2 (YSZ). This led to the development of ceramic anode materials as mentioned before, like Ni/YSZ, due to their longer TPB length, reasonable electronic conductivity, and catalytic activity[129]. Nevertheless, the durability of Ni/YSZ anodes remains a persistent issue due to problems such as coking, electrode poisoning[40,75,130,131], phase change, and mechanical failure brought about by high temperatures[14,132].

The cathode materials are required to possess high catalytic activity, electronic and ionic conductivity, CTE compatibility, chemical stability, and cost-effectiveness, similar to anode materials[14,75]. Perovskite materials have shown great potential for use in both anode and cathode materials[133]. Since 1973, $La_{1-x}Srx MnO3 - \delta$ (LSM) has been the most extensively studied cathode material for SOFCs to date.

The electrolyte material used in SOFCs must possess high ionic conductivity for O^{2-} ions and CTE compatibility with the electrode material. YSZ material was first discovered in the 1890s by Nernst, who observed high O^{2-} conductivity at high temperatures. Among various YSZ materials, 8 mol.% Y_2O_3 stabilized ZrO_2 (8YSZ) has been shown to exhibit the highest ionic conductivity.

A solid understanding of electrochemistry principles is crucial for the effective testing of SOFCs. In fundamental research aimed at exploring new materials, unit button cell testing is a commonly used method. The experimental setup in this study involves a button cell composed of Ni/YSZ|YSZ|LSM/YSZ|LSM, with two different Ni/YSZ compositions. The electrode thickness is approximately 20 μm, and the electrolyte is 150 μm thick. The anode and cathode have radii of 1 cm and 0.5 cm, respectively, resulting in an active electrode area of about 0.5 cm^2. This setup allows for accurate measurement and characterization of the cell's performance, making it an effective tool for testing SOFCs.

To prepare the anode, a mixture of NiO and YSZ is synthesized and tested in weight ratios of 40:60 wt.% and 60:40 wt.%. The anode and cathode are screen-printed onto the YSZ pellet, followed by sequential sintering at 1300 °C and 1000 °C for 2 hours. Prior to sintering, both materials are heated to 400 °C and held for 2 hours to allow for the evaporation of organic substances. The heating rate is maintained at 2 °C/min and the cooling rate at 5 °C/min. This process results in a well-prepared anode and cathode, which can be used to assemble the button cell for subsequent testing of SOFCs.

Once sintering is complete, a silver wire is attached to the anode and cathode sides using a silver paste. The SOFC unit is then sealed onto an alumina tube using ceramic sealant, with care taken to prevent large strains that could cause electrode cracking and gas leakage. To do this, the sealant is allowed to dry at room temperature for approximately 2 hours before the test kit is raised to 200 °C at a rate of 0.5 °C/min and then brought up to the test temperature at a rate of 1 °C/min. Finally, the test kit is inserted into a programmable furnace and connected to an electrochemical station via the silver wire for testing. For more detailed information on the slurry preparation procedure for the button SOFC, please refer to **Paper IV**.

4.1.2 Testing of SOFC

Fig. 4.1 illustrates the experimental setup used for testing the SOFCs. The setup includes an alumina tube and ceramic sealant, which are selected for their compatibility with the CTE of the electrode and electrolyte. It is crucial to ensure that the anode material is fully reduced by feeding it with 5% H_2 during the temperature-raising phase. In addition, to maintain the fuel's flow state, it is humidified using a bubbler filled with water, which is checked periodically. The exhaust gas outlet is vented to the air via two bubblers to prevent backflow after cooling. During testing, two samples are evaluated within a temperature range of 700-800 °C, with an increment of 50 °C per step and a heating rate of 5 °C/min.

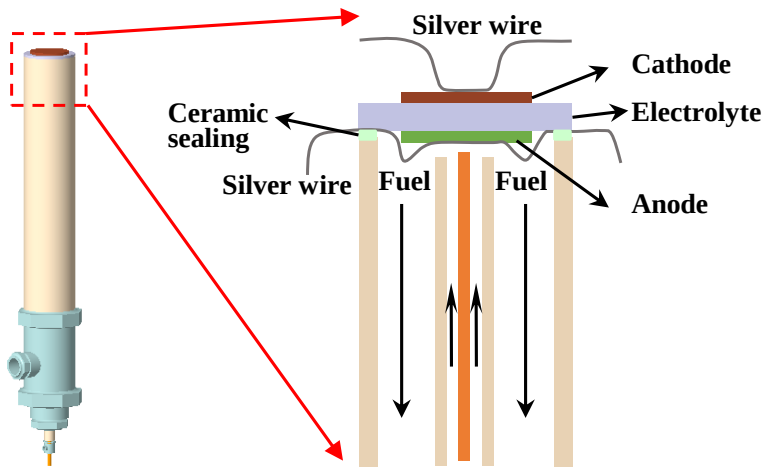

Figure 4.1: The schematic of the unit SOFC testing kit with the cross-section illustration; the anode is sealed inside the alumina tube, while the cathode is left open to the air; the silver wires are attached to the anode and cathode side stretched out to connect the electrochemical work station.

Electrochemical impedance spectroscopy (EIS) is a powerful technique used to study the electrode processes of SOFCs, including charge transfer and gas transport. To obtain reliable and accurate results, it is crucial to maintain gas tightness during the testing process. In addition, current-voltage-power (IVP) measurements can be performed to obtain the open circuit voltage (OCV), which serves as a criterion to verify the gas tightness of the testing kit. A high OCV value, typically over 1 V, indicates good gas tightness. To ensure reliable electrode-electrolyte and silver wire-electrode contacts, proper preparation and sealing techniques are employed, such as the use of ceramic sealant and controlled drying. The quality of these contacts is essential to achieve accurate results and avoid false readings.

4.1.3 Characterization and reconstruction

The operation of SOFCs involves a complex interplay of phenomena across multiple length scales, spanning from atomic/molecular interactions to stack/system-level engineering. At the nanoscale, the fundamental electrochemical reactions take place, while at the micrometre to sub-micrometre length scales, transport processes in the electrode are critical for proper SOFC function. Slow transport processes can lead to polarization and voltage losses. Therefore, a deep understanding of the microscale behaviour of SOFCs is essential for designing and optimizing porous electrode materials and comprehending the overall performance of the system.

To fully understand the nature of 3D percolation, it is essential to obtain 3D microstructure data. Stereology and quantitative microscopy theory[68] can provide valuable microstructure information such as porosity, TPB length, and particle size distribution. However, these techniques have limitations and cannot fully reveal the complex 3D microstructure of the material. Therefore, additional methods, such as focused ion beam FIB-SEM[134], X-ray CT[135] are necessary to obtain more comprehensive 3D microstructure information.

Figure 4.2 illustrates the schematic of the FIB-SEM apparatus and the reconstruction process. To obtain 2D slice images, the anode sample needs to be reprocessed and cut using FIB-SEM. After that, the images are cropped, filtered, and thresholded to generate binarized images for 3D reconstruction.

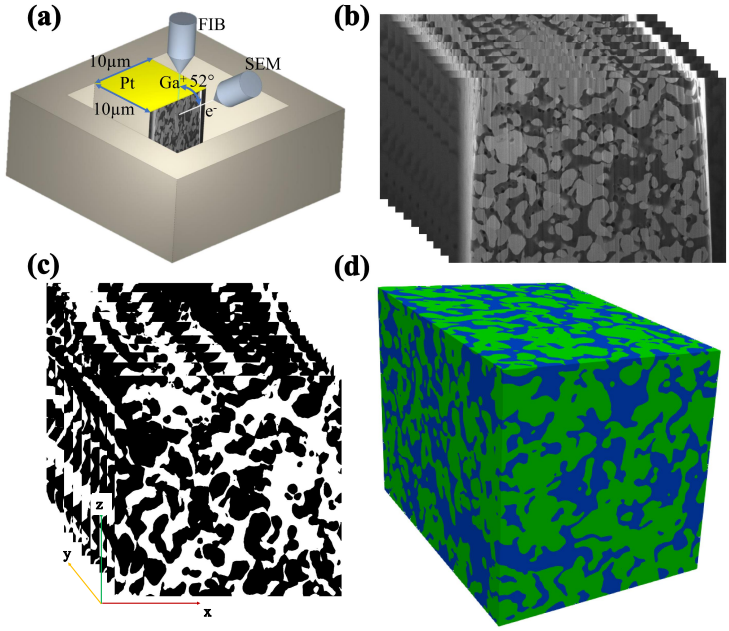

Figure 4.2: (a)The schematic of FIB-SEM; (b) the original 2D images; (c) processed 2D image; (d) reconstructed microstruture of the Ni-YSZ anode.

4.2 Tortuosity

Most ageing issues, including poisoning, coking, Ni agglomeration, and phase change will lead to microstructure degradation. To improve the lifetime and performance of SOFCs, researchers are continuously developing new materials, such as perovskites, not only for SOFCs but also for other energy applications[136]. Additionally, optimizing the microstructure of the porous electrode also for enhancing the performance and durability of SOFCs. This can be achieved through techniques such as infiltration, evolution, and different fabrication methods[48,137,138]. By employing such approaches, the optimized electronic/ionic conductivity, and catalytic activity can be achieved. One of the concerns that also should be considered is the transport of species in the porous material.

To enable electrochemical reactions, a sufficient concentration of species is required. At high current densities, however, inadequate gas transport in the porous medium can result in concentration overpotential. The porous

medium's complex and tortuous nature often leads to a decrease in diffusion, making it crucial to understand the microstructure's impact on transport. To this end, effective transport properties, including diffusion coefficient, thermal conductivity, electronic, and ionic conductivity, can be linked to bulk transport properties using the M-factor[139,140].

$$\Phi^{eff} = M\Phi_0, \tag{4.1}$$

where Φ^{eff} and Φ_0 are the effective transport properties, with the M-factor can be defined as:

$$M = \frac{\varepsilon^n}{\tau^m}, \tag{4.2}$$

where m and n are empirical constants. Some models also take into account the constriction factor β and the percolation factor P[141].

$$M = \frac{(\varepsilon P)^b \beta^c}{\tau^d}. \tag{4.3}$$

Tortuosity, τ, is defined as the actual tortuous path length (inlet and outlet) Δl divided by the Euclidean distance (straight through the path length between inlet and outlet) Δx.

$$\tau_{geo} = \frac{\Delta l}{\Delta x}. \tag{4.4}$$

Several methods exist for defining the length of a tortuous path, including the shortest path length[142], the average path length[143], and flux-based algorithms that use effective path length[144]. However, there is often confusion in the literature between tortuosity and tortuosity factors. Tortuosity is defined based on the assumption that the porous medium consists of sinuous but parallel capillaries or pores, as proposed by Epstein[145]. In this definition, tortuosity is the ratio of the average pore length, L_e, to the Euclidean distance, L.

Epstein later introduced the tortuosity factor, which is derived by considering one-dimensional pressure-driven viscous flow through a porous medium. The pressure drop is calculated using the Hagen-Poiseuille equation, which describes the fully developed laminar flow of a single-phase Newtonian fluid through a typical capillary of hydraulic diameter D_h and length L_e.

$$-\Delta P = \frac{b\mu L_e v}{D_h^2}, \tag{4.5}$$

The distinction between the effective pore velocity v and the interstitial axial velocity u_i can be made by relating the superficial velocity u with u_i.

This relationship yields the tortuosity factor, $(L_e/L)^2$, while the tortuosity is defined as L_e/L. A more detailed derivation can be found in reference[145]. It is important to note that both definitions of tortuosity assume a constant effective cross-sectional area normal to the flow direction. In the current study, the main focus is to compare different calculation methods, we will be using tortuosity for consistency.

4.3 Calculation methods

4.3.1 Experiment based

Determining the tortuosity of a porous medium can be a challenging task if detailed geometric information is not available. There are experimental methods that can be used to determine the effective properties of the medium. These include diffusion cell experiments[146] and electrochemical measurements[142]. In the study, empirical methods and numerical methods are used rather than experiment methods.

4.3.2 Porosity tortuosity relationships

Porosity-tortuosity relationships provide a straightforward approach to calculating tortuosity based solely on porosity. One widely used model is the Bruggeman model[147,148], which is given by Eq. (4.6). This model assumes a porous medium with a connected conductive phase containing uniform-sized insulating spherical particles. It is important to note that the Bruggeman correlation is only valid when the insulating (obstruction) phase is present in a low-volume fraction (saturated porous) and is represented by random isotropic spheres or cylinders. Typically, a correction factor of $\gamma \approx 1$ and a Bruggeman exponent of $\alpha \approx 1.5$ are used[142,148].

$$\tau_{Brug} = \gamma \varepsilon^{1-\alpha} \tag{4.6}$$

The Millington and Quirk model[149] assumes that the porous media is homogeneous and consists of spherical solids that interpenetrate with each other and spherical pores that also interpenetrate with each other. In a saturated porous medium, the tortuosity can then be expressed as:

$$\tau_{Mill} = \varepsilon^{-1/3} \tag{4.7}$$

It is noted that, for both Bruggeman, Millington and Quirk model, the porous media are assumed to be saturated. For a cluster of randomly arranged spheres, Maxwell's porosity-tortuosity correlation gives the expression shown in Eq. (4.8) [150].

$$\tau_{Max} = \frac{3 - \varepsilon}{2} \tag{4.8}$$

4.3.3 3D microstructure based approach

As discussed in Section 4.2, advanced tomography methods have greatly facilitated the availability of 3D microstructure data. By utilizing the 3D volume, microstructure parameters such as TPB length, connectivity, phase distribution, porosity, particle size distribution, and tortuosity can be obtained [142]. There are different methods to calculate tortuosity based on 3D microstructure data. The first approach is the path-length-based method, which involves finding the path length across the porous medium. The second approach is the flux-based algorithm, which uses either voxel-based or mesh-based simulations.

Path-length approaches are considered the most direct and straightforward approach for calculating tortuosity as they align with the initial definition of tortuosity presented in Section 4.2. In this approach, algorithms such as the centroid pore method, fast marching method, and distance propagation method are applied to the voxel domain of interest to find the shortest path from the inlet plane to the outlet plane [142]. However, the shortest path may not necessarily reflect the effective path length, and therefore, the average path length is also used in other literature [143]. Additionally, a CFD simulation-based path-length approach is also used, which calculates the path length of fluid streamlines in the porous medium [151,152]. In this study, we utilize the CFD simulation combined path-length approach for comparison.

The voxel-based approach solves the flux equation in the voxel domain, making it highly dependent on the resolution of the 2D images [153]. The accuracy and calculation time of the voxel-based approach is greatly impacted by the size of the voxels in the 3D image. However, compared to mesh-based flux simulation, the voxel-based approach is relatively more accurate since it preserves more detailed geometric information without the need for a smoothing process by normal reconstruction. For more information about the voxel-based approach, refer to **Paper IV**.

Chapter 5

Results and discussions

In this section, the SOFC performance test results are analyzed. The real 3D microstructure of the anode is constructed, followed by comparing different approaches for tortuosity calculations. The results found that even based on 3D real microstructure, the tortuosity value may differ greatly due to different assumptions. In order to further develop SOFC model, we comprehensively studied a fully coupled 3D planar single-channel solid oxide fuel cell (SOFC) model by comparing different forms of electrochemical reaction kinetics and gas diffusion models which is the content of **Paper II**. Furthermore, we investigate the impact of microstructure on the performance of the SOFC, based on the model developed previously. Lastly, the thermal stress of the SOFC with different sealant compositions is analyzed by multiphysics simulations. Further research focused on the interface thermal stress simulations based on simplified interface contact.

5.1 SOFC test and microstructure characterization

5.1.1 SOFC test results

The anode composition of 60:40 wt.% (CP1) and 40:60 wt.% (CP2) is prepared and tested. The detailed procedure for electrode preparation and test rig setup is in **Paper IV**. Fig. 5.1 shows the electrochemical impedance spectroscopy (EIS) and polarization power (IVP) plots for CP1 and CP2. The impedance is lower for CP1 than CP2, which means better electrical

performance. Therefore, SOFC with CP1 anode has a higher power density and a higher current density. The big electrical difference between CP1 and CP2 is that the former has a higher content of NiO, which is reduced to Ni acting as a catalyst for fuel oxidation. In addition, high NiO also leads to high volume change, since the reduction of NiO to Ni will lead to volume shrink. Therefore, the microstructure is altered, which affects both charge and gas transport. This, on the other hand, restricts the NiO content, as Ni agglomeration will decrease the catalyst performance. A uniform catalyst (Ni) distribution will yield a high current density.

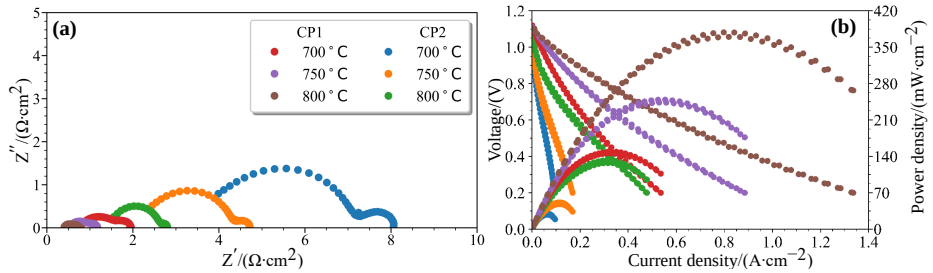

Figure 5.1: (a) The Nyquist plots measured at 0.7V for CP1 and CP2 measured at different temperatures; (b) The IVP for CP1 and CP2 at different temperatures. (the same colour legend is used for each composition and its testing temperature).

In addition, EIS plot fitting and DRT analysis is also carried out to obtain the equivalent circuit (EC) and analyze the dynamic processes in the electrode. After the test, FIB-SEM is used to characterize the SOFC and the anode electrode. The cross-section of the button SOFC shows in Fig.5.2 (a), with a dense electrolyte and a porous cathode and anode. The trench cut around the anode is shown in Fig. 5.2 (b). 2D slice images of the anode through FIB-SEM are used to calculate the tortuosity.

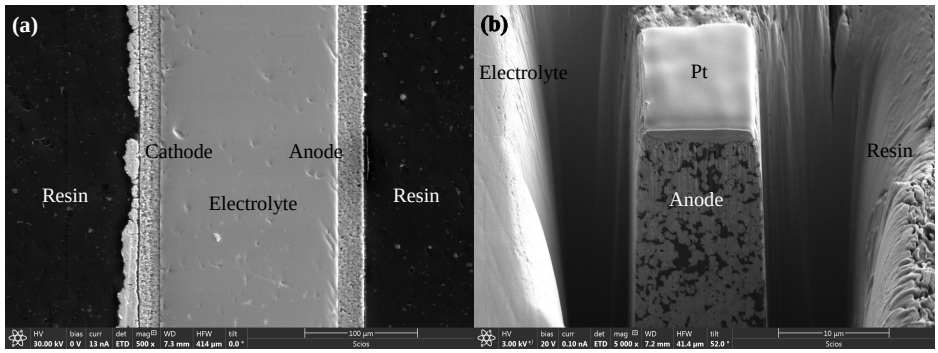

Figure 5.2: SEM image of (a) cross-section of the polished cell; (b) trench milled on the anode.

There are three methods used to calculate the anode pore tortuosity, namely, porosity-tortuosity relationship, voxel-based and path-length-based methods as introduced before. The porosity used for the porosity-tortuosity relationship is evaluated by voxel-based methods. There are three porosity-tortuosity relationships. i.e., Bruggeman model, Millington and Quirk model, and Maxwell model. The other 2 methods are based on microscale tomography data. The 2D slice images are used for the voxel-based method, and the porosity is also evaluated. The 3D volume structure is used for the path-length-based approach. A detailed description of these methods is given in **Paper IV**.

Table 5.1: tortuosity calculated using different methods; The porosity-tortuosity relationship give single value; The x-direction (thickness) and y-direction (radial) are calculated for Voxel-based and path-length-based method; The path-length-based method counted minimum, maximum, and average path length.

Method	CP1						CP2					
Brug	1.58						1.69					
Mill	1.36						1.41					
Max	1.30						1.33					
Voxel		2.00			2.07			2.44			2.29	
Path	1.14	2.00	1.42	1.21	2.00	1.42	1.18	2.02	1.47	1.17	2.34	1.46

Table 5.1 shows the tortuosity calculated with different methods for CP1 and CP2. It can be seen that CP1 with high NiO content has lower tortuosity, which is favourable for gas transport. The porosity-tortuosity relationship underestimates the tortuosity. Besides, it can only give a single value. While the voxel-based and path-length-based approaches can calculate the tortuosity in different directions. It can be seen that the x-direction

and y-direction have similar tortuosity values for the voxel-based approach, with values of 2.00 and 2.07 respectively. While CP2 has a relatively larger discrepancy between the x-direction and the y-direction, with values of 2.44 and 2.29. This means that CP1 has a more homogeneous pore structure, although the pixel number may affect the results. It is interesting that the longest path length gets the tortuosity similar to the voxel-based approach. While the shortest and average path lengths get too low a tortuosity value. Besides, the path-length-based approach uses a shorter time than the voxel-based approach. A high electronic phase (Ni) in the anode, will improve the electric performance of SOFC. The parametric sweep of the electrode composition also demonstrates that there is an optimum electronic phase volume fraction between 0.25-0.28.

5.2 Investigation of electrochemical reaction kinetics and diffusion models

5.2.1 Model settings

The geometry of the SOFC model supported by anodes has been described in detail in **Paper II**. The model incorporates governing equations for the transport of charges, gas species, momentum, and heat. The fuel inlet composition consists of H_2 and H_2O, with a molar fraction of H_2 being 0.9. The air inlet consists of O_2 and N_2, with an O_2 molar fraction of 0.21. The counter-flow mode has been employed at the fuel and air inlet. The fixed gas flow velocity has been set at the inlet of the air and fuel channel. The outflow boundary condition has been set to a constant atmospheric pressure of 1 atm. The inlet temperature has been set at 727°C, while the outlet has been set to normal flow, meaning that the heat flows out of the domain only by convection. The voltage on the cathode side has been set to 0.7 V, and the anode has been set to a ground condition of 0 V.

5.2.2 Case setup for electrochemical reaction kinetics

Case 1

Two different BV equations and the exchange current density i_0 are used in this study. The Cases are differentiated based on whether the concentration term is included or not, and the BV equation is further divided

into activation-controlled and diffusion-controlled models. The activation-controlled BV equation for Case 1 is given by:

$$i = a_v i_0 \left[\exp\left(\frac{\beta_a F \eta}{RT}\right) - \exp\left(\frac{-\beta_c F \eta}{RT}\right) \right], \tag{5.1}$$

where i_0 is the exchange current density defined in Eq. (2.16)[154]. The pre-exponential factor is 6.54×10^{11} $1/\Omega/\mathrm{m}^2$ and 2.35×10^{11} $1/\Omega/\mathrm{m}^2$ for the anode and cathode, respectively. The activation energy is 140 kJ/mol and 137 kJ/mol for the anode and cathode, respectively. The symmetry factor β_a and β_c for the anodic and cathodic reactions are set to 0.5. The active surface area $a_{v,a}$ and $a_{v,c}$ for the anode and cathode is 0.4785×10^6 1/m and 1×10^6 1/m, respectively, and is kept constant for all Cases.

Case 2

For Case 2, the same BV equation is used as Case 1, as shown in Eq. 5.1. However, the exchange current density for the anode and cathode is different[111,112]:

$$i_{0,a} = k_a \left(\frac{p_{H_2}}{p_{H_2,ref}}\right)^A \left(\frac{p_{H_2O}}{p_{H_2O,ref}}\right)^B \exp\left(\frac{-E_a}{RT}\right), \tag{5.2}$$

$$i_{0,c} = k_c \left(\frac{p_{O_2}}{p_{O_2,ref}}\right)^C \exp\left(\frac{-E_c}{RT}\right), \tag{5.3}$$

where k_a and k_c are the pre-exponential factors with values of 3.5×10^2 $\mathrm{A/m}^2$ and 3.35×10^5 $\mathrm{A/m}^2$, respectively. E_a and E_c are the activation energies for the anodic and cathodic reactions, which are 70 kJ/mol and 130 kJ/mol, respectively. The exponents A, B, and C are 0.41, 0.4, and 0.3, respectively.

Case 3

For Case 3, the diffusion-controlled BV equation is used. The current density for the anode and cathode can be defined as:

$$i_{v,a} = a_{v,a} i_{0,a} \left[\frac{x_{H_2}}{x_{H_2,ref}} \exp\left(\frac{\alpha_a F \eta}{RT}\right) - \frac{x_{H_2O}}{x_{H_2O,ref}} \exp\left(\frac{-\alpha_c F \eta}{RT}\right) \right]. \tag{5.4}$$

$$i_{v,c} = a_{v,c} i_{0,a} \left[\frac{x_{O_2}}{x_{O_2,ref}} \exp\left(\frac{\alpha_a F \eta}{RT}\right) - \exp\left(\frac{-\alpha_c F \eta}{RT}\right) \right]. \tag{5.5}$$

The exchange current density $i_{0,a/c}$ remains the same as in Case 1 with identical parameters, but the concentration term is now incorporated in

the anode and cathode exponent term instead of the exchange current density. It is important to note that the inclusion of species concentration terms in these kinetic models accounts for the concentration polarization phenomenon.

Diffusion models based on Case 2

The Maxwell-Stefan description of diffusion flux is shown in Eq. (3.20), followed by considering porous structure and Knudsen diffusion. The Fick model relates the diffusion flux to the gradient of the species concentration, which can be written as:

$$\mathbf{j}_i = -\rho D_i \nabla \omega_i - \rho \omega_i D_i \frac{\nabla Mn}{Mn} + \rho \omega_i \sum_k \frac{M_i}{Mn} D_k \nabla x_k, \tag{5.6}$$

The diffusion coefficient D_i can also be adapted to account for porous structure impact and Knudsen diffusion. Therefore, four diffusion models are compared quantitatively compare its effect on SOFC performance.

5.2.3 Velocity and species distribution

To ensure the accuracy of the numerical simulations, a mesh independence analysis is conducted by examining the temperature profile along the fuel flow direction in the middle of the anode. The mesh is generated by sweeping face elements in the flow direction. The temperature profile for various mesh densities is presented in Figure 2 and the velocity profile is first analyzed in Figure 3 in **Paper II**.

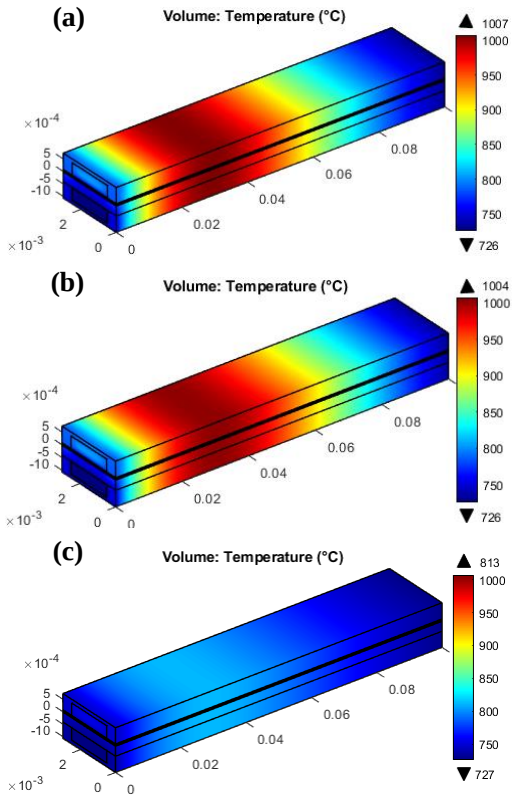

Figure 5.3: The temperature profile for (a) Case 1; (b) Case 2, and (c) Case 3.

Fig. 5.3 displays the temperature profiles of Cases 1, 2, and 3. As the air inlet velocity is higher, the high-temperature zone is located near the fuel inlet. The temperature magnitudes for Case 1 and Case 2 are similar, while Case 3 shows an obviously lower temperature. Typically, the velocity in the air channel is higher than the fuel channel to ensure sufficient O_2 supply and heat dissipation. The average velocity magnitudes in the fuel channel are 0.18 m/s, 0.41 m/s, and 0.2 m/s for Case 1, 2, and 3, respectively.

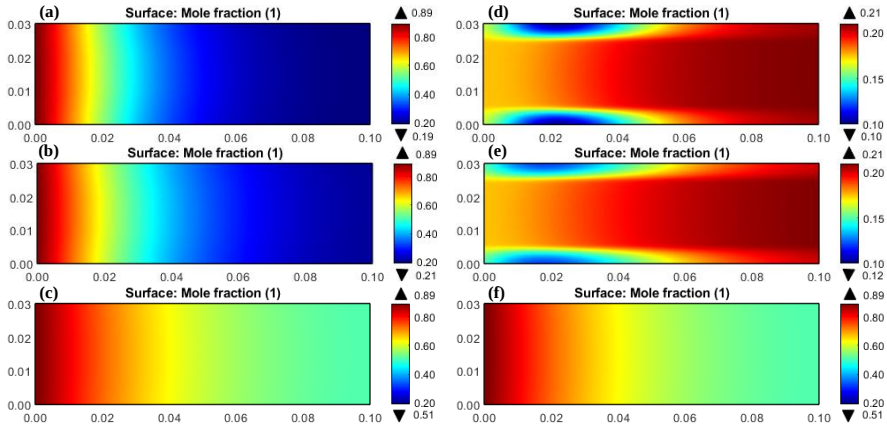

Figure 5.4: (a-c) H_2 distribution at the interface of anode/electrolyte (IAE) for Case 1-3; and (d-f) O_2 distribution at the interface of cathode/electrolyte (ICE) for Case 1-3.

Figure 5.4 displays the H_2 and O_2 distribution at the interface of anode/electrolyte (IAE) and cathode/electrolyte (ICE). The colour map scales are set equal to facilitate comparison. The counterflow model is adopted, with the fuel inlet on the left-hand side and the air inlet on the right-hand side. It is observed that Case 1, which utilizes the activation-controlled BV equation, exhibits a more significant O_2 deficiency. On the other hand, Case 3, which employs the same exchange current density as Case 1 but a diffusion-controlled BV equation, demonstrates the lowest gas consumption. Notably, both Case 1 and Case 2 display higher O_2 consumption near the outlet of the air channel, beneath the interconnect rib, in contrast to Case 3. This is because there is a higher electrochemical reaction rate for Case 1 and 2 compared to Case 3. Furthermore, O_2 is less diffusive than H_2, despite the higher velocity, which can be improved by reducing the thickness of the interconnect ribs.

5.2.4 Current density

The exchange current density represents the current density at which the forward and backward reactions are in equilibrium. In Fig. 5.5 (a-c), the exchange current density at the ICE is shown for Cases 1-3. The figure indicates that the exchange current density is higher where the molar fraction of O_2 is low, indicating that electrochemical reactions are more intense in those regions. The high local current density is also observed near the fuel inlet, but it is higher near the interconnect ribs where the electron

transport path is shorter than in the middle of the channel. However, the high exchange current density spreads across the electrode. The average exchange current density values are 0.65, 0.52, and 0.09 A/cm^2 for Cases 1, 2, and 3, respectively. The local current density is the current density evaluated by the BV equation without multiplying the activation surface area (a_v). The average local current density values are 0.82, 1.38, and 0.26 A/cm^2 for Cases 1, 2, and 3, respectively. Although Case 1 and 3 use the same expression for exchange current density, the latter has a lower local current density value, while Case 2 has the highest, as can be seen from the figure. These results demonstrate that the activation-controlled BV equation gives a higher reaction rate compared to the diffusion-controlled Case. When considering gas composition in the exchange current density for Case 2, there is an even higher local current density compared to Case 1.

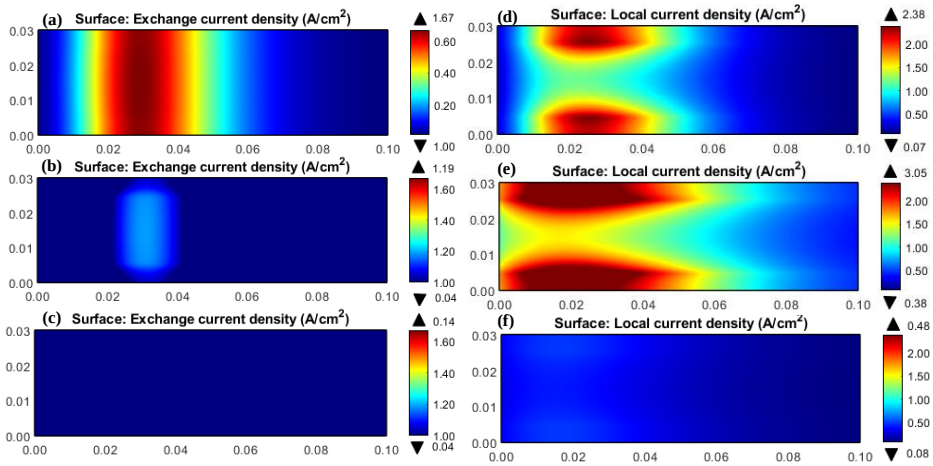

Figure 5.5: (a-c) Exchange current density and (d-f)local current density at the interface of cathode/electrolyte (ICE) for Case 1-3.

The electronic and ionic current density distribution at the ICE is evaluated by the charge balance equation, as discussed in Chap. 3, and shown in Fig. 5.6. The distribution of electronic and ionic current density is similar to that of the local current density, with higher values near the fuel inlet. However, the electronic current density is higher near the interconnect and does not diffuse under it. In contrast, the high ionic current density at the IAE (not shown in the figure) further diffuses under the interconnect. This is because the cathode side, interconnect hinders O_2 diffusion, while

the small H_2 molecule on the anode side is not affected. The high ionic current density distributes under the interconnect for both ICE and IAE is the same, independent of O_2 deficiency. The average electronic current density is 1.40, 1.48, and 0.60 A/cm^2 for Cases 1, 2, and 3, while the average ionic current density is 0.39, 0.36, and 0.16 A/cm^2, respectively. Case 2 has the highest electronic and ionic current density, reflecting its higher local current density, and higher gas consumption than Case 3 (Fig. 5.4). The exchange current density for diffusion-controlled BV is the lowest and therefore has the lowest electronic and ionic current density.

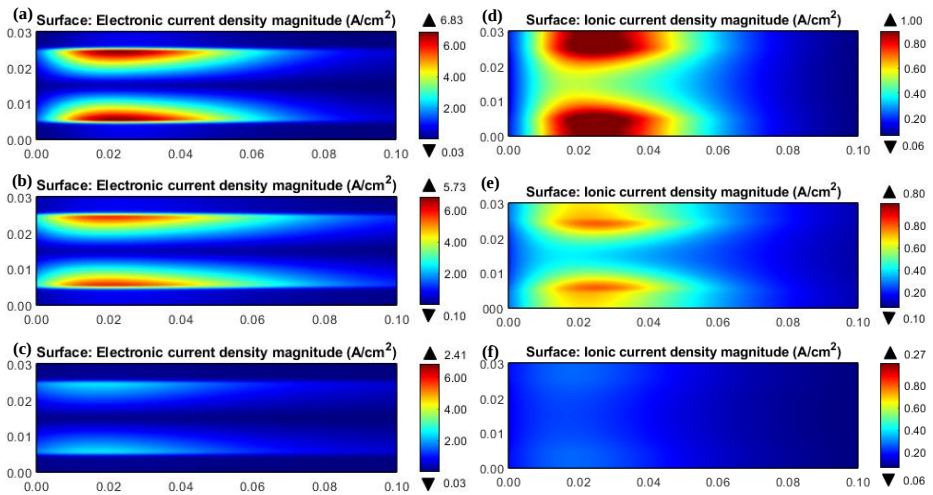

Figure 5.6: (a-c) Electronic current density and (d-f) ionic current density at the interface of cathode/electrolyte (ICE) for Case 1-3.

Fig. 5.7 illustrates the activation polarization at the IAE and ICE for Cases 1-3. Case 1 shows the lowest value at IAE, while Case 2 shows the highest. On the other hand, at ICE, Case 3 exhibits the highest activation overpotential, while Case 2 has the lowest. In addition, for Cases 1 and 3, the activation overpotential is higher at ICE compared to IAE. For Cases 1 and 2, the lowest activation overpotential appears in the middle of the SOFC, where the highest value appears near the inlet. However, IAE and ICE have different activation overpotential distributions for Case 3, which is mainly due to the lower current density.

During a typical IV curve, shown in Fig. 2.1, the activation overpotential is high when the current density is low. This is because the low reaction rate requires more energy to break the energy barrier, resulting in a voltage

loss in the SOFC, which is reflected by the highest activation overpotential near the fuel inlet at ICE for Case 3.

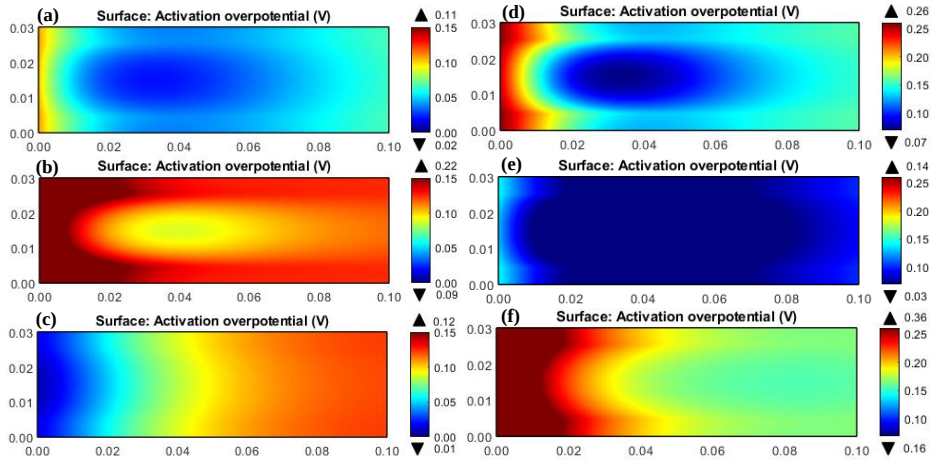

Figure 5.7: The activation overpotential at (a-c) the IAE, and (d-f) the ICE for Cases 1-3.

5.2.5 Diffusion models comparison

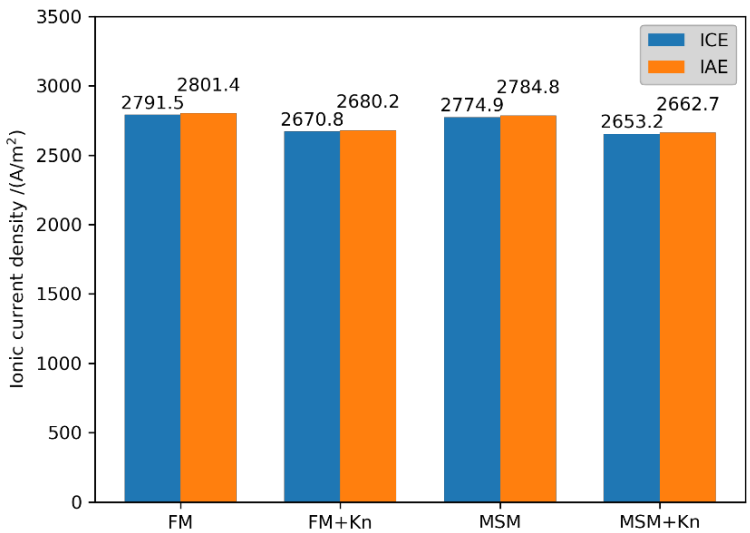

Figure 5.8: The average ionic current density at IAE and ICE for the Fick model (FM) and Maxwell-Stefan model (MSM) with and without considering Knudsen diffusion.

The average ionic current density both at IAE and ICE for FM and MSM predict almost the same values. Therefore, gas consumption, concentration overpotential and temperature are almost the same for each model considered. The consideration of pressure and multicomponent diffusion for MSM compared with FM has a negligible impact on the overall cell performance prediction. The ionic current density decreased for both models with the same magnitude after considering Knudsen diffusion. The results demonstrate that Knudsen diffusion must be considered, while FM is more efficient.

5.2.6 Discussions

The present Case study compares the results of different electrochemical kinetic models, i.e., the exchange current density and the BV equation. Case 1, without considering the gas species in the kinetic model, results in a high current density but encounters an O_2 deficiency. Case 2, which still uses the activation-controlled BV equation but considers the gas composition in the exchange current density, gives a slightly higher current density and relatively lower O_2 deficiency. However, the diffusion-controlled BV equation for Case 3, with the same exchange current density as Case 1 gives a lower current density, resulting in a slow electrochemical reaction rate. For Cases 1 and 3, the parameters such as pre-exponential factor, activation energy, symmetry factor, and activation surface area can be adjusted to fine-tune the model. For Case 2, the extra exponent in the exchange current density can also be adjusted. Since Case 2 incorporates the species concentration, it implicitly included the concentration overpotential. Case 3 considers the gas composition effect but has a slow reaction rate. Therefore, Case 2 is selected for further simulations.

5.3 Micro-structure impact on SOFC performance

5.3.1 Model construction and validation

The simulation setup used in this study is consistent with that described in Chapter 3, with the same governing equations and numerical methods. The geometry size parameters and mesh details are described in **Paper III**, and the mesh has been selected based on a thorough mesh independence

investigation. The electrochemical kinetic model used is the same as in Case 2, with the exception of the active surface area and the activation energy at the anode, which have been adjusted according to the parameters listed in Table 2 of **Paper III**. The numerical polarization curve obtained from the simulation is then compared with experimental data to validate the accuracy of the model.

5.3.2 Case setup

Table 5.2 summarizes Case setup with different tortuosity values for gas (τ_g), ions (τ_{ion}), and electrons (τ_{ele}) transport. In base Case A, all porous electrodes have a tortuosity of 10. Based on Case A, Case B decreases the tortuosity τ_{ion} for ion transport in the active anode and cathode to 5. Case C sets the tortuosity for electron transport τ_{ele} in the active and support layers to 5. Similarly, the gas transport tortuosity τ_g in the active and support layers is changed to 5 in the Case of D. Finally, Case E decreases all tortuosity to 5 with the same changes in each individual Case.

Table 5.2: Tortuosity changes for different Cases.

Case	A	B	C	D	E
τ_g	10	10	10	5	5
τ_{ion}	10	5	10	10	5
τ_{ele}	10	10	5	10	5

In addition to the Cases mentioned earlier, we conducted a parametric study to investigate the impact of electrode composition. Specifically, we varied the electronic phase volume fraction in the anode and cathode active layers in Group 1, ranging from 0.2 to 0.35 with a step increase of 0.025. The porosity of both layers remained constant at 0.3, resulting in a change in the ionic phase volume fraction along with the electronic phase volume fraction.

Similarly, in Group 2, we changed the electronic phase volume fraction in the anode and cathode support layers from 0.6 to 0.4 with a step decrease of 0.04. Since the support layer only contains an electronic phase and pores, the porosity changed correspondingly with the electronic phase volume fraction.

5.3.3 Temperature

Figure 5.9 illustrates the 3D temperature profile for Case A. It is evident that the temperature rise is significant near the fuel inlet and gradually decreases until the air inlet. One contributing factor is the higher air velocity compared to fuel, resulting in greater temperature convection. The maximum temperature observed in Case A is 900 °C. Among all Cases, Case E exhibited the highest temperature rise, with a maximum temperature of 940° C, achieved by simultaneously reducing the tortuosity of gas and charge transfer. However, individually reducing tortuosity resulted in a comparable temperature rise, with maximum temperatures of 908°C, 909°C, and 907°C for Cases B, C, and D, respectively. Further analysis of the gas distribution was conducted.

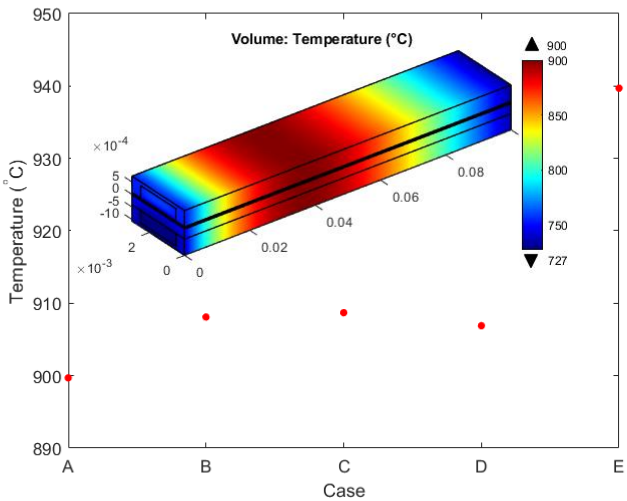

Figure 5.9: Maximum temperature variation for all Cases, and embedded 3D temperature distribution profile for Case A.

5.3.4 Gas consumption

Fig. 5.10 illustrates the molar fraction distribution for H_2 and O_2 at the anode and cathode sides. The maximum molar fraction is observed at the inlet, which gradually decreases along the flow direction. As a counter-flow mode is employed, the concentration reduces in the opposite direction. Under the interconnect, the O_2 concentration almost reaches zero due to the hinder effect from the interconnect. The H_2 utilization based on the outlet

and inlet molar fraction reaches 84.01%. For Cases, B, C, D, and E, the H_2 utilization values were 88.42%, 89.45%, 89.07%, and 96.54%, respectively. The electric transport tortuosity has a greater impact on fuel consumption than the gas and ionic transport tortuosity. This is due to ionic conduction only occurring in the active layer, while electric conduction occurs in both the active and support layers resulting in slightly higher fuel consumption.

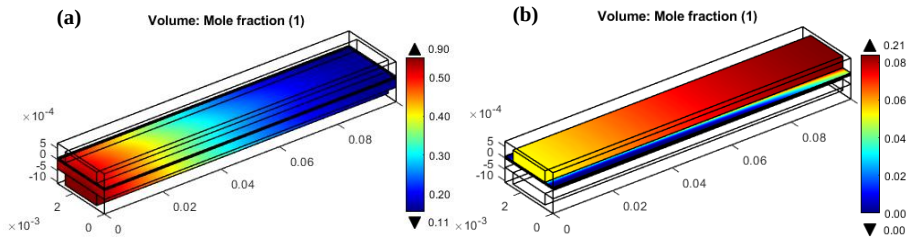

Figure 5.10: (a) H_2 molar fraction distribution and (b) O_2 molar fraction distribution in the SOFC for the base Case A.

5.3.5 Current density and overpotential

Fig. 5.11 displays the ionic and electronic current density for Case A. The high current density is predominantly distributed under or near the interconnect, with the current density decreasing along the gas channel from the fuel inlet (i.e., the left-hand side of the figure). This indicates that the electrochemical reaction rate is highest near the fuel inlet, resulting in elevated temperatures and gas consumption in that region. As a result, an O_2 deficiency is observed under the interconnect rib.

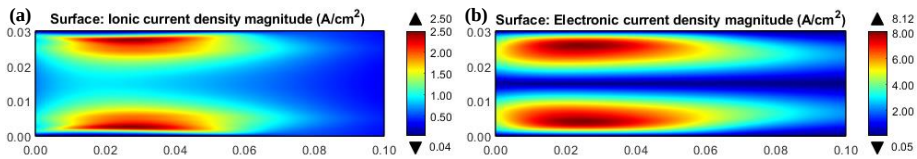

Figure 5.11: (a) Ionic current density at the middle of the electrolyte for Case A; and (b) electronic current density at the IAE for Case A.

Fig. 5.12 displays the average electronic current density at IAE, the average ionic current density at the middle of the electrolyte, and the average H_2

molar fraction at the outlet. The average ionic current density for each Case is 0.98, 1.07, 1.06, 0.99, and 1.17 A/cm^2, while the average electronic current density exhibits greater variability with changes in tortuosity. The average electronic current density at the IAE for each Case is 3.34 A/cm^2, 3.64 A/cm^2, 4.11 A/cm^2, 3.04 A/cm^2, and 4.23 A/cm^2. Decreasing the ionic and electronic tortuosity individually for Case B and C results in higher electronic current density, whereas decreasing the gas transport tortuosity for Case D leads to a lower electronic current density compared to Case 1. The average ionic current density for Case D is almost the same as Case 1. Case E exhibits the highest ionic and electronic current density among all Cases, resulting in the lowest average outlet H_2 molar fraction. High current density indicates a high electrochemical reaction rate and, therefore, more gas consumption. The results demonstrate that decreasing the electronic transport tortuosity has a greater impact on the electrochemical reaction, but the combined decrease of tortuosity has a much higher impact.

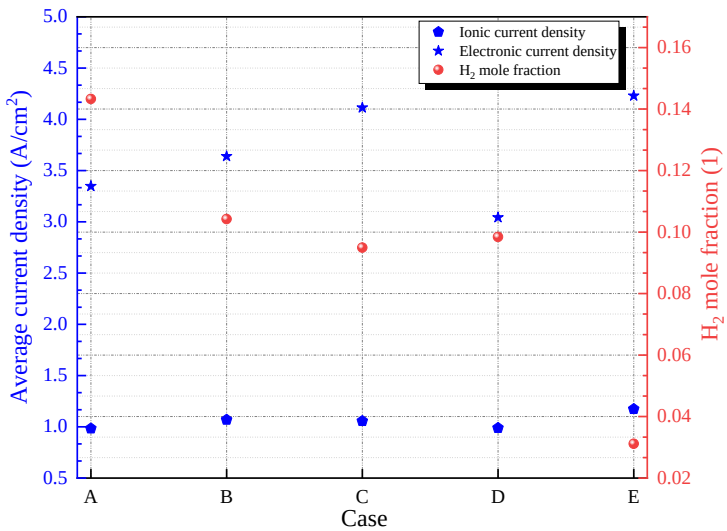

Figure 5.12: The average current density and outlet average H_2 molar fraction variation with different Cases.

The flow of electrons is from the anode to the cathode, while O^{2-} ions are generated at the cathode and transported through the electrolyte to the anode. When the tortuosity is decreased, it facilitates faster transport of species from the anode to the cathode TPB. However, the average ionic current density does not change significantly compared with the average electronic current density, due to the thinner ionic contained elec-

trode thickness compared to the total electrode thickness. Moreover, the electrolyte, being the main ionic conductor, implies that the ionic current density can be significantly improved by increasing the electrolyte conductivity. On the other hand, the electronic phase is thicker than the ionic phase, which means that the decrease in tortuosity has a more significant impact on the electronic current density.

Fig. 5.13 illustrates the activation overpotential for Case A, which shows that the high activation overpotential is mainly concentrated at the fuel inlet side, and it decreases along the flow direction. The high activation overpotential also appears at the IAE and ICE, as depicted in Fig. 5.13(c) and (d). The activation overpotential near/under the interconnect is higher than in the middle and lateral regions, as seen from Fig. 5.13(d). Notably, in the middle, an elliptical shape forms where a low activation overpotential appears.

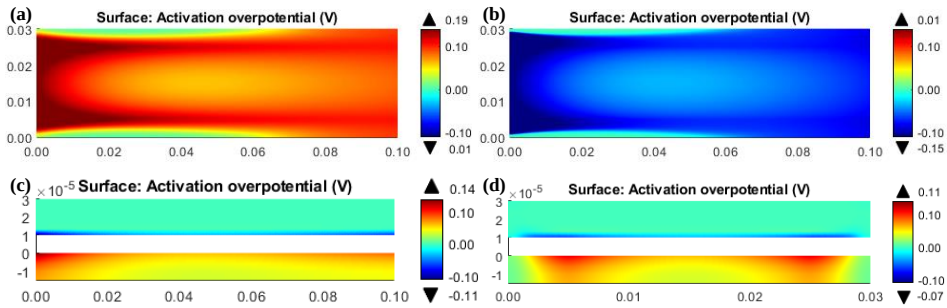

Figure 5.13: (a) Activation overpotential at IAE; (b) activation overpotential at ICE; (c) activation overpotential at the middle of the SOFC along flow direction; (d) activation overpotential at the middle of the SOFC perpendicular to the flow direction (bottom is the active anode, top is the active cathode).

The high activation overpotential means that more energy is needed to overcome the energy barrier for the electrochemical reaction to proceed. This energy is reflected as voltage loss of the cell potential. The activation overpotential variation at the middle of the SOFC along the flow direction can be found in **Paper III**. The gas transport tortuosity change has a negligible effect on the maximum overpotential compared with a decrease in the electron and ion transport tortuosity. The decrease in tortuosity tends to increase the activation overpotential. The average activation is evaluated together for the active anode and cathode, with a value of 0.023 V, 0.023 V, 0.025 V, 0.023 V, and 0.029 V for Cases A-E. Therefore, the high activation comes along with a high electronic current density. As

the electronic current density increases, the electrochemical reaction rate increases, more electrons are needed, and there need more species involved, which need more energy to overcome the energy barrier. This further leads to voltage loss, i.e., high activation overpotential.

5.3.6 Composition impact

A further parametric sweep is performed for anode and cathode compositions. The first group increase the volume fraction of the electronic phase in the active anode and active cathode and keep the porosity constant. In general, the increase of the electronic phase in the active electrode will lead to the increase of electronic current density, but the ionic current density decreased consequently, and vice versa. Therefore, there is a trading-off point, which has the highest electric performance. It is noted that the porosity of the active electrode also affects the electric potential.

In conclusion, tortuosity is an important parameter which affects the electric performance of the SOFC. Therefore, a proper method must be used to evaluate the tortuosity of the porous material. Besides, the volume fraction in the electrode also has an optimum value. The results stressed the importance of microstructure optimization. The Optimization must come with a suitable approach to characterize the microstructure quantitatively. In order to design electrode architecture, experiments, 3D reconstruction-based characterization, and Multiphysics simulation are promising approaches.

5.4 Thermal stress simulations

5.4.1 Button SOFC with different sealant materials

This part of the simulation is based on the experimental data of different sealant materials. The glass sealant is prepared by doping with different ZrO_2. The CTE, gas leakage rate and morphology are investigated in **Paper V**. The geometry size, governing equations, and boundary conditions are also described in detail.

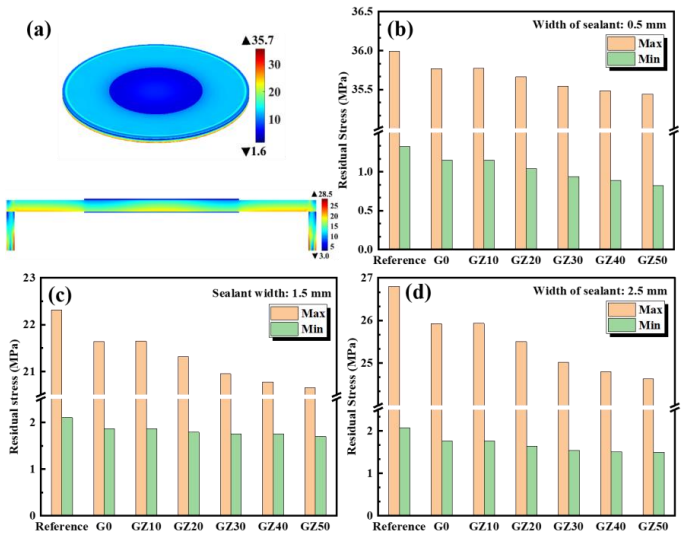

Figure 5.14: (a) Residual stress profile of the button SOFC and at the cross-section for reference Case; (b-d) Maximum and minimum residual stress in the sealant G0-GZ50, with sealant width of 0.5 mm, 1.5mm, and 2.5 mm.

Fig. 5.14 shows the residual stress distribution with different sealant materials. The residual stress is relatively small in the electrodes due to the porous structure, which absorbs the thermal expansion. The stress in the sealant is not evenly distributed, therefore, the maximum and minimum stress is obtained. The width of the sealant materials is changed to consider the geometry effect on the stress. The difference between the maximum and minimum stress for the width of 1.5 mm is smaller than that of 0.5 mm and 2.5 mm. Larger contact areas tend to spread the stress more evenly and also with a lower value. The stress decrease with the increase of the doping content. But considering the CTE match, and the leakage test results, GZ10 is considered as a suitable sealant material.

5.4.2 Thermal stress at micro interface

The interface of the electrode and electrolyte is not closely bonded, rather, it consists of individual contact points. Besides, the cathode material always suffers from Cr poisoning due to the high temperature. At high temperatures, the Cr in the metallic interconnect evaporated, diffused and react with the cathode material. Therefore, the contact area of the cathode and electrolyte with and without Cr poisoning are also investigated based on a micro-scale SOFC.

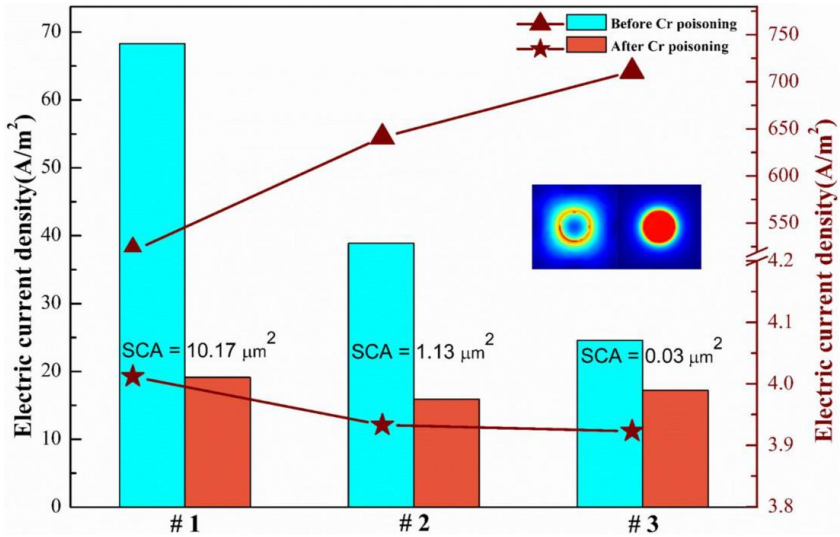

Figure 5.15: The maximum electrical current density (ECD) with different contact modes at the interface between cathode and contact layer (ICCL) (bar graph), out the surface of cathode (OSC) (line graph), with an embedded ECD distribution the # 1 Case before and after Cr poisoning.

Figure 5.15 displays the maximum electrical current density variation with different contact sites with the same area, and also with and without Cr poisoning. From the embedded figure, high current density distribute at the rim of the contact sites compared with poisoned ones distributed across the whole contact area. The maximum current density of a single contact area decreases with the increase of the contact site's number with and without Cr poisoning at the interface between the cathode and contact layer. Before poisoning, the outer surface electrical current density increase with the increase of the contact number. While the current density decreases with the increase of the contact sites after Cr Poisoning.

Chapter 6

Summary and outlook

6.1 Summary

This thesis investigates the impact of microstructure on the performance of SOFCs. The effect of solid phase volume fraction on SOFC performance is examined to achieve this. Two-anode composition assembled button SOFC are tested and characterized using FIB-SEM to obtain 2D cross-sectional images of the anode. There are three methods to characterize the tortuosity of the porous material. The path length-based approach is based on the reconstructed 3D anode porous microstructure. Specifically, CFD simulation is performed to obtain the streamline, with MATLAB script used to obtain the maximum, minimum, and average path length. The 2D images are utilized for the voxel-based approach to obtain both tortuosity and porosity, and the porosity is then utilized in porosity-tortuosity relationships.

Meanwhile, several electrochemical kinetics models and diffusion models are implemented on a planar SOFC to select a suitable model. The activation-controlled and diffusion-controlled BV equations are utilized, along with two kinetic expressions for exchange current density. After selecting the appropriate model, the activation-controlled BV equation with modified exchange current density is chosen to explore the impact of tortuosity variation on gas consumption and electrical properties. The results can be concluded as follows:

- Experiment is conducted to interrogate the anode composition impact on a button SOFC performance. The results reveal that the high NiO

content greatly improves the electric performance. This is due to the fact that there is a more percolated electronic phase for CP2 with higher NiO content. Besides, there is also an increased three-phase boundary, which allows electrochemical reaction happens. The FIB-SEM is used to get the porous anode tomography structure, i.e., 2D slice images. The 2D slice images are used to generate the 3D volume structure for CFD simulation. The results show that the porosity-tortuosity model underestimates the tortuosity compared with the base Case (voxel-based approach). The longest path length gives a similar tortuosity value to the voxel-based approach. The shortest and average path length also gives a lower tortuosity value.

- Electrochemical kinetics Case 1 and Case 2 use the activation-controlled BV equation. While Case 2 uses exchange current density, which considers species concentration. The change in the exchange current density has a limited impact on the SOFC electrical performance. Both Case 1 and Case 2 have similar average exchange current density and electrical/ionic current density. But for that Case 2 there is a more uniform current density. Case 3, uses the diffusion-controlled BV equation to give the lowest electrochemical reactions. However, it gives the highest activation overpotential. The results show that considering a gas concentration in the BV equation is essential. Therefore, Case 2 is used for further simulations.

- Case 2 with a modified exchange current density BV equation is selected for investigation of microstructure impact on SOFC performance. The results show that the electrical performance can be improved by decreasing the electric and ionic conducting tortuosity. A high current density caused by a decrease in electronic conducting tortuosity increases activation overpotential. The gas transport tortuosity has a lower impact on the electrical performance compared with the electrical and ionic conduction tortuosity. The variation of the average ionic current density is smaller compared with the electronic current density. With fixed porosity in the anode and cathode active layer, there is a trade-off point for the electronic phase and ionic phase volume fraction. The same applies to the anode and cathode support layers.

- Thermal stress of different sealant materials used for a button SOFC is studied. The results show that modified glass sealant has good hermiticity and better mechanical properties at high temperatures. Thermal stress distribution at the interface of the cathode/electrolyte

is also investigated. With the increase of contact sites in between, the current density increases. Meanwhile, the thermal stress of single contact sites also increases. Cr poisoning greatly decreases the performance of the SOFC.

6.2 Outlook

The SOFC can be used for power generation, but when combined with solar and wind power generation, the SOEC mode can be used for carbon capture. The existing primary energy can be efficiently utilized while the exhaust gas CO_2 can be converted to fuels. In such a way, near-zero CO_2 emissions can be achieved in the near future. From the development of materials to the balance of plants, however, there are still many fundamental problems, such as the short life and high cost. While electrode material must balance a spectrum of criteria such as cost, thermal/chemical stability, electronic conductivity, gas diffusion and catalytic activity. These criteria determine the SOFC performance throughout all operation regimes. Therefore, starting from the design of electrode materials, the following research works can be conducted:

Mesoscale

Quantitatively analysing the porous electrodes through advanced microstructural characterization techniques such as nano-CT and FIB-SEM tomography. The key parameters such as porosity, tortuosity, TPB density, and electronic/ionic/gas phase percolation, are closely related to the electrochemical performance that can be obtained. However, the microstructure parameters are not independent of each other, which means improving one property may come with sacrificing others. Therefore, combining electrochemical tests and tomography techniques can help design high-performance electrodes, by controlling the processing and environmental parameters such as particle size distribution, compositions, deposition methods, and sintering. Besides, long-term characterize microstructure altering and its relationship with SOFC performance also can be investigated.

In order to further quantitatively understand the microstructure impact on the SOFC performance, mesoscale modelling can be used to establish this relationship. There is numerical modelling work based on real microstructure through multiphysics FEM simulations[155]. Further work can be done to establish a relationship between microstructure parameters and electro-

chemical performance to help the design of efficient electrode materials.

Macroscale

With optimized electrode materials, there are still engineering difficulties to build and scale up the SOFC for large and commercial applications. The existing research involves macroscale mechanical optimization, gas channel design and lifetime predictions which need single-cell and stack-level models. However, on the stack level, it is notoriously expensive as it takes too much time even for stationary simulations. Therefore, next research also can be conducted regarding establishing a sufficiently accurate stack model while saving computational cost.

More efficient approach

Machine learning appears extremely hot topic regarding its application in many research areas due to its robustness and high efficiency. The application mainly focused on performance evaluation, lifetime prediction and application monitoring[156]. Recently interesting work has been done to generate microstructure based on SOFC performance using machine learning[157]. Therefore, connecting processing parameters, microstructure performance and macroscale performance can be achieved through machine learning as long as there are sufficient experimental data. This in turn, greatly facilitates the design of SOFC.

References

[1] OWID, Energy consumption per capita worldwide from 1965 to 2021 (in kilowatt-hours) (2022).

[2] UNDESA, World economic situation and prospects (2022).

[3] O. W. in Data, Years of fossil fuel reserves left (2020).

[4] B. S. R. of World Energy, Energy development (2022).

[5] B. S. R. of World Energy, European council, 24-25 march 2022 (2022).

[6] I. E. Agency, World energy outlook (2022).

[7] N. Kannan, D. Vakeesan, Solar energy for future world:-a review, Renewable and Sustainable Energy Reviews 62 (2016) 1092–1105.

[8] A. Mahesh, K. S. Sandhu, Hybrid wind/photovoltaic energy system developments: Critical review and findings, Renewable and Sustainable Energy Reviews 52 (2015) 1135–1147.

[9] S.-J. Kim, W. Koo, M.-J. Shin, Numerical and experimental study on a hemispheric point-absorber-type wave energy converter with a hydraulic power take-off system, Renewable Energy 135 (2019) 1260–1269.

[10] R. J. Pearson, S. Takeda, Review of approaches to fusion energy, Commer Fusion Energy.

[11] H. Stančin, H. Mikulčić, X. Wang, N. Duić, A review on alternative fuels in future energy system, Renewable and sustainable energy reviews 128 (2020) 109927.

[12] R. Steinberger-Wilckens, Introduction to fuel cell basics, in: Advances in Medium and High Temperature Solid Oxide Fuel Cell Technology, Springer, 2017, pp. 1–29.

[13] Z. Yang, Z. Lei, B. Ge, X. Xiong, Y. Jin, K. Jiao, F. Chen, S. Peng, Development of catalytic combustion and co2 capture and conversion technology, International Journal of Coal Science & Technology 8 (3) (2021) 377–382.

[14] S. Zarabi Golkhatmi, M. I. Asghar, P. D. Lund, A review on solid oxide fuel cell durability: Latest progress, mechanisms, and study tools, Renewable and Sustainable Energy Reviews 161 (2022) 112339.

[15] F. S. da Silva, T. M. de Souza, Novel materials for solid oxide fuel cell technologies: A literature review, International Journal of Hydrogen Energy 42 (41) (2017) 26020–26036.

[16] M. Z. Khan, M. T. Mehran, R.-H. Song, J.-W. Lee, S.-B. Lee, T.-H. Lim, A simplified approach to predict performance degradation of a solid oxide fuel cell anode, Journal of Power Sources 391 (2018) 94–105.

[17] A. Benyoucef, D. Klein, C. Coddet, B. Benyoucef, Development and characterisation of (ni, cu, co)-ysz and cu-co-ysz cermets anode materials for sofc application, Surface and Coatings Technology 202 (10) (2008) 2202–2207.

[18] C. M. Grgicak, M. M. Pakulska, J. S. O ' Brien, J. B. Giorgi, Synergistic effects of ni1xcox-ysz and ni1xcux-ysz alloyed cermet sofc anodes for oxidation of hydrogen and methane fuels containing h2s, Journal of Power Sources 183 (1) (2008) 26–33.

[19] X. Wu, Y. Tian, J. Zhang, W. Zuo, X. Kong, J. Wang, K. Sun, X. Zhou, Enhanced electrochemical performance and carbon anti-coking ability of solid oxide fuel cells with silver modified nickel-yttrium stabilized zirconia anode by electroless plating, Journal of Power Sources 301 (2016) 143–150.

[20] K. Sasaki, K. Susuki, A. Iyoshi, M. Uchimura, N. Imamura, H. Kusaba, Y. Teraoka, H. Fuchino, K. Tsujimoto, Y. Uchida, et al., H2s poisoning of solid oxide fuel cells, Journal of the Electrochemical Society 153 (11) (2006) A2023.

[21] J. Van herle, T. Horita, T. Kawada, N. Sakai, H. Yokokawa, M. Dokiya, Low temperature fabrication of (y,gd,sm)-doped ceria electrolyte, Solid State Ionics 86-88 (1996) 1255–1258, proceedings of the 10th International Conference on Solid State Ionics.

[22] A. J. Jacobson, Materials for solid oxide fuel cells, Chemistry of Materials 22 (3) (2010) 660–674.

[23] Y. Liu, L. Jia, J. Li, B. Chi, J. Pu, J. Li, High-performance ni in-situ exsolved ba(ce0.9y0.1)0.8ni0.2o3-/gd0.1ce0.9o1.95 composite anode for sofc with long-term stability in methane fuel, Composites Part B: Engineering 193 (2020) 108033.

[24] N. Peng, J. T. Irvine, A. G. Fitzgerald, Synthesis and crystal structure of the distorted perovskite sr 0.97 nbo 3 determined by high resolution powder neutron diffraction, Journal of Materials Chemistry 8 (4) (1998) 1033–1038.

[25] S. Hui, A. Petric, W. Gong, Stability and conductivity of perovskite oxides under anodic conditions, ECS Proceedings Volumes 1999 (1) (1999) 632.

[26] P. Slater, J. Irvine, T. Ishihara, Y. Takita, High-temperature powder neutron diffraction study of the oxide ion conductor la0. 9sr0. 1ga0. 8mg0. 2o2. 85, Journal of Solid State Chemistry 139 (1) (1998) 135–143.

[27] T. McColm, J. Irvine, B site doped strontium titanate as a potential sofc substrate, Ionics 7 (1-2) (2001) 116–121.

[28] S. Primdahl, J. Hansen, L. Grahl-Madsen, P. Larsen, Sr-doped lacro3 anode for solid oxide fuel cells, Journal of the Electrochemical Society 148 (1) (2001) A74.

[29] G. Pudmich, B. A. Boukamp, M. Gonzalez-Cuenca, W. Jungen, W. Zipprich, F. Tietz, Chromite/titanate based perovskites for application as anodes in solid oxide fuel cells, Solid State Ionics 135 (1-4) (2000) 433–438.

[30] P. R. Slater, D. P. Fagg, J. T. Irvine, Synthesis and electrical characterisation of doped perovskite titanates as potential anode materials for solid oxide fuel cells, Journal of Materials Chemistry 7 (12) (1997) 2495–2498.

[31] S. Hui, A. Petric, Evaluation of yttrium-doped srtio3 as an anode for solid oxide fuel cells, Journal of the European Ceramic Society 22 (9-10) (2002) 1673–1681.

[32] P. Holtappels, J. Bradley, J. Irvine, A. Kaiser, M. Mogensen, Electrochemical characterization of ceramic sofc anodes, Journal of the electrochemical society 148 (8) (2001) A923.

[33] J. Irvine, Perovskite oxide anodes for sofcs, Perovskite oxide for solid oxide fuel cells (2009) 167–182.

[34] N. Q. Minh, Ceramic fuel cells, Journal of the American Ceramic Society 76 (3) (1993) 563–588.

[35] S. Tao, J. T. Irvine, A redox-stable efficient anode for solid-oxide fuel cells, Nature materials 2 (5) (2003) 320–323.

[36] S. Tao, J. T. Irvine, Study on the structural and electrical properties of the double perovskite oxide srmn 0.5 nb 0.5 o 3- δ, Journal of Materials Chemistry 12 (8) (2002) 2356–2360.

[37] S. Tao, J. Canales-Vázquez, J. T. Irvine, Structural and electrical properties of the perovskite oxide sr2fenbo6, Chemistry of Materials 16 (11) (2004) 2309–2316.

[38] C. Bernuy-Lopez, M. Allix, C. A. Bridges, J. B. Claridge, M. J. Rosseinsky, Sr2mgmoo6-δ: structure, phase stability, and cation site order control of reduction, Chemistry of materials 19 (5) (2007) 1035–1043.

[39] C. Sun, U. Stimming, Recent anode advances in solid oxide fuel cells, Journal of Power Sources 171 (2) (2007) 247–260.

[40] Z. Yang, M. Guo, N. Wang, C. Ma, J. Wang, M. Han, A short review of cathode poisoning and corrosion in solid oxide fuel cell, International Journal of Hydrogen Energy 42 (39) (2017) 24948–24959.

[41] A. Barbucci, M. Viviani, M. Panizza, M. Delucchi, G. Cerisola, Analysis of the oxygen reduction process on sofc composite electrodes., Journal of applied electrochemistry 35 (4).

[42] J. A. Kilner, M. Burriel, Materials for intermediate-temperature solid-oxide fuel cells, Annual Review of Materials Research 44 (2014) 365–393.

[43] C. Sun, R. Hui, J. Roller, Cathode materials for solid oxide fuel cells: a review, Journal of Solid State Electrochemistry 14 (2010) 1125–1144.

[44] A. Jun, J. Kim, J. Shin, G. Kim, Perovskite as a cathode material: a review of its role in solid-oxide fuel cell technology, ChemElectroChem 3 (4) (2016) 511–530.

[45] B. Kamecki, G. Cempura, P. Jasinski, S.-F. Wang, S. Molin, Tuning electrochemical performance by microstructural optimization of the nanocrystalline functional oxygen electrode layer for solid oxide cells, ACS Applied Materials & Interfaces.

[46] S. U. Rehman, A. Shaur, H.-S. Kim, D. W. Joh, R.-H. Song, T.-H. Lim, J.-E. Hong, S.-J. Park, S.-B. Lee, Effect of transition metal doping on the sintering and electrochemical properties of gdc buffer layer in sofcs, International Journal of Applied Ceramic Technology 18 (2) (2021) 511–524.

[47] S. Gamble, Fabrication–microstructure–performance relationships of reversible solid oxide fuel cell electrodes–review, Materials Science and Technology 27 (10) (2011) 1485–1497.

[48] P. A. Connor, X. Yue, C. D. Savaniu, R. Price, G. Triantafyllou, M. Cassidy, G. Kerherve, D. J. Payne, R. C. Maher, L. F. Cohen, R. I. Tomov, B. A. Glowacki, R. V. Kumar, J. T. S. Irvine, Tailoring sofc electrode microstructures for improved performance, Advanced Energy Materials 8 (23) (2018) 1800120.

[49] O. Kwon, S. Joo, S. Choi, S. Sengodan, G. Kim, Review on exsolution and its driving forces in perovskites, Journal of Physics: Energy 2 (3) (2020) 032001.

[50] K. Kousi, C. Tang, I. S. Metcalfe, D. Neagu, Emergence and future of exsolved materials, Small 17 (21) (2021) 2006479.

[51] B. Hua, M. Li, Y.-F. Sun, J.-H. Li, J.-L. Luo, Enhancing perovskite electrocatalysis of solid oxide cells through controlled exsolution of nanoparticles, ChemSusChem 10 (17) (2017) 3333–3341.

[52] J. W. Shin, D. Go, S. H. Kye, S. Lee, J. An, Review on process-microstructure-performance relationship in ald-engineered sofcs, Journal of Physics: Energy 1 (4) (2019) 042002.

[53] Z. Li, H. Zhang, H. Xu, J. Xuan, Advancing the multiscale understanding on solid oxide electrolysis cells via modelling approaches: A review, Renewable and Sustainable Energy Reviews 141 (2021) 110863.

[54] S. N. Rashkeev, M. V. Glazoff, Atomic-scale mechanisms of oxygen electrode delamination in solid oxide electrolyzer cells, international journal of hydrogen energy 37 (2) (2012) 1280–1291.

[55] Y. Sun, C. Wang, Y. Chen, Molecular dynamics simulations of the deformation behavior of gadolinia-doped ceria solid electrolytes under tensile loading, Journal of power sources 233 (2013) 131–138.

[56] D. S. Gunn, J. A. Purton, S. Metz, Monte carlo simulations of gadolinium doped ceria surfaces, Solid State Ionics 324 (2018) 128–137.

[57] C. Yang, R. Guo, X. Jing, P. Li, J. Yuan, Y. Wu, Degradation mechanism and modeling study on reversible solid oxide cell in dual-mode —a review, International Journal of Hydrogen Energy.

[58] S. B. Beale, M. Andersson, C. Boigues-Muñoz, H. L. Frandsen, Z. Lin, S. J. McPhail, M. Ni, B. Sundén, A. Weber, A. Z. Weber, Continuum scale modelling and complementary experimentation of solid oxide cells, Progress in energy and combustion science 85 (2021) 100902.

[59] D. Zhang, A. Bertei, F. Tariq, N. Brandon, Q. Cai, Progress in 3d electrode microstructure modelling for fuel cells and batteries: transport and electrochemical performance, Progress in Energy 1 (1) (2019) 012003.

[60] L. Holzer, D. Wiedenmann, B. Münch, L. Keller, M. Prestat, P. Gasser, I. Robertson, B. Grobéty, The influence of constrictivity on the effective transport properties of porous layers in electrolysis and fuel cells, Journal of materials science 48 (2013) 2934–2952.

[61] D. Wiedenmann, L. Keller, L. Holzer, J. Stojadinović, B. Münch, L. Suarez, B. Fumey, H. Hagendorfer, R. Brönnimann, P. Modregger, et al., Three-dimensional pore structure and ion conductivity of porous ceramic diaphragms, AIChE Journal 59 (5) (2013) 1446–1457.

[62] L. Holzer, B. Iwanschitz, T. Hocker, L. Keller, O. Pecho, G. Sartoris, P. Gasser, B. Muench, Redox cycling of ni–ysz anodes for solid oxide fuel cells: Influence of tortuosity, constriction and percolation factors on the effective transport properties, Journal of Power Sources 242 (2013) 179–194.

[63] A. Bertei, E. Ruiz-Trejo, K. Kareh, V. Yufit, X. Wang, F. Tariq, N. Brandon, The fractal nature of the three-phase boundary: A

heuristic approach to the degradation of nanostructured solid oxide fuel cell anodes, Nano Energy 38 (2017) 526–536.

[64] Q. Fu, Z. Li, W. Wei, F. Liu, X. Xu, Z. Liu, Performance degradation prediction of direct internal reforming solid oxide fuel cell due to ni-particle coarsening in composite anode, Energy Conversion and Management 233 (2021) 113902.

[65] J. Zhu, Z. Lin, Degradations of the electrochemical performance of solid oxide fuel cell induced by material microstructure evolutions, Applied Energy 231 (2018) 22–28.

[66] A. He, J. Gong, J. Onishi, N. Shikazono, Three-dimensional topology optimization of ni-ysz anode for solid oxide fuel cells via multiphase level-set method, Nano Energy 103 (2022) 107817.

[67] B. Bosio, F. R. Bianchi, Multiscale modelling potentialities for solid oxide fuel cell performance and degradation analysis, Sustainable Energy & Fuels 7 (1) (2023) 280–293.

[68] P. R. Shearing, D. J. L. Brett, N. P. Brandon, Towards intelligent engineering of sofc electrodes: a review of advanced microstructural characterisation techniques, International Materials Reviews 55 (6) (2010) 347–363.

[69] M. E. Lynch, D. Ding, W. M. Harris, J. J. Lombardo, G. J. Nelson, W. K. Chiu, M. Liu, Flexible multiphysics simulation of porous electrodes: Conformal to 3d reconstructed microstructures, Nano Energy 2 (1) (2013) 105–115.

[70] X. Lu, T. Li, A. Bertei, J. I. Cho, T. M. Heenan, M. F. Rabuni, K. Li, D. J. Brett, P. R. Shearing, The application of hierarchical structures in energy devices: new insights into the design of solid oxide fuel cells with enhanced mass transport, Energy & Environmental Science 11 (9) (2018) 2390–2403.

[71] A. Sciazko, Y. Komatsu, A. Nakamura, Z. Ouyang, T. Hara, N. Shikazono, 3d microstructures of solid oxide fuel cell ni-ysz anodes with carbon deposition, Chemical Engineering Journal 460 (2023) 141680.

[72] N. H. Menzler, D. Sebold, Y. J. Sohn, S. Zischke, Post-test characterization of a solid oxide fuel cell after more than 10 years of stack testing, Journal of Power Sources 478 (2020) 228770.

[73] M. C. Williams, S. D. Vora, G. Jesionowski, Worldwide status of solid oxide fuel cell technology, ECS Transactions 96 (1) (2020) 1.

[74] R. Perry, Report on the status of the solid oxide fuel cell program (2019).

[75] N. Mahato, A. Banerjee, A. Gupta, S. Omar, K. Balani, Progress in material selection for solid oxide fuel cell technology: A review, Progress in Materials Science 72 (2015) 141–337.

[76] K. Kendall, Introduction sofcs, in: High-temperature Solid Oxide Fuel Cells for the 21st Century: Fundamentals, Design and Applications, Springer, 2016, pp. 1–22.

[77] M. R. Terner, J. A. Schuler, A. Mai, D. Penner, On the conductivity degradation and phase stability of solid oxide fuel cell (sofc) zirconia electrolytes analysed via xrd, Solid State Ionics 263 (2014) 180–189.

[78] N. Shaigan, W. Qu, D. G. Ivey, W. Chen, A review of recent progress in coatings, surface modifications and alloy developments for solid oxide fuel cell ferritic stainless steel interconnects, Journal of Power Sources 195 (6) (2010) 1529–1542.

[79] M. Guo, Y. Jin, R. Zhang, Z. Yang, S. Peng, Low leakage rate of silicate glass modified with al2o3 for solid oxide fuel cell, Journal of the European Ceramic Society 42 (7) (2022) 3264–3270.

[80] A. Tabish, H. Patel, P. Chundru, J. Stam, P. Aravind, An sofc anode model using tpb-based kinetics, International Journal of Hydrogen Energy 45 (51) (2020) 27563–27574.

[81] W. H. Kan, A. J. Samson, V. Thangadurai, Trends in electrode development for next generation solid oxide fuel cells, Journal of Materials Chemistry A 4 (46) (2016) 17913–17932.

[82] The electrolysis of water, Journal of Electroanalytical Chemistry 476 (1) (1999) 92–93.

[83] S. Grigoriev, V. Fateev, D. Bessarabov, P. Millet, Current status, research trends, and challenges in water electrolysis science and technology, International Journal of Hydrogen Energy 45 (49) (2020) 26036–26058, progress in Hydrogen Production and Utilization.

[84] H. Davy, On some new phenomena of chemical changes produced by electricity, partic- ularly the decomposition of the fixed alkalis, and

the exhibition of the new substances, which constitute their bases, Phil. Trans.Roy.Soc.Lond 98 (1808) 1–45.

[85] I. Riess, Mixed ionic–electronic conductors—material properties and applications, Solid State Ionics 157 (1) (2003) 1–17, proceedings of the 6th International Symposium on Systems with Fast Ionic Transport (ISSFIT).

[86] K. A. Kuterbekov, A. V. Nikonov, K. Z. Bekmyrza, N. B. Pavzderin, A. M. Kabyshev, M. M. Kubenova, G. D. Kabdrakhimova, N. Aidarbekov, Classification of solid oxide fuel cells, Nanomaterials 12 (7). doi:10.3390/nano12071059.

[87] J. W. Fergus, Sealants for solid oxide fuel cells, Journal of Power Sources 147 (1) (2005) 46–57.

[88] J. Wu, X. Liu, Recent development of sofc metallic interconnect, Journal of Materials Science Technology 26 (4) (2010) 293–305.

[89] L. Tan, X. Dong, C. Chen, Z. Gong, M. Wang, Diverse system layouts promising fine performance demonstration: A comprehensive review on present designs of sofc-based energy systems for building applications, Energy Conversion and Management 245 (2021) 114539.

[90] P. Atkins, L. Jones, Chemical principles: The quest for insight, Macmillan, 2007.

[91] A. L. Dicks, D. A. Rand, Fuel cell systems explained, John Wiley & Sons, 2018.

[92] S. Giddey, S. Badwal, A. Kulkarni, C. Munnings, A comprehensive review of direct carbon fuel cell technology, Progress in Energy and Combustion Science 38 (3) (2012) 360–399.

[93] A. Buonomano, F. Calise, M. D. d' Accadia, A. Palombo, M. Vicidomini, Hybrid solid oxide fuel cells–gas turbine systems for combined heat and power: A review, Applied Energy 156 (2015) 32–85.

[94] F. Ramadhani, M. Hussain, H. Mokhlis, S. Hajimolana, Optimization strategies for solid oxide fuel cell (sofc) application: A literature survey, Renewable and Sustainable Energy Reviews 76 (2017) 460–484.

[95] W. Winkler, Chapter 3: Thermodynamics, in: K. Kendall, M. Kendall (Eds.), High-Temperature Solid Oxide Fuel Cells for the 21st Century (Second Edition), second edition Edition, Academic Press, Boston, 2016, pp. 51–83.

[96] S. Balasubramanian, A. Z. Weber, Continuum, macroscopic modeling of polymer-electrolyte fuel cells, in: Physical Multiscale Modeling and Numerical Simulation of Electrochemical Devices for Energy Conversion and Storage, Springer, 2016, pp. 91–149.

[97] D. Ferrero, A. Lanzini, M. Santarelli, Solid oxide fuel cells modeling, in: Advances in medium and high temperature solid oxide fuel cell technology, Springer, 2017, pp. 291–342.

[98] I. EGG Technical Services, Fuel Cell Handbook (Seventh Edition), U.S. Department of Energy, 2004.

[99] M. Ni, M. K. Leung, D. Y. Leung, Parametric study of solid oxide fuel cell performance, Energy Conversion and Management 48 (5) (2007) 1525–1535.

[100] Y. Patcharavorachot, A. Arpornwichanop, A. Chuachuensuk, Electrochemical study of a planar solid oxide fuel cell: Role of support structures, Journal of Power Sources 177 (2) (2008) 254–261.

[101] M. Andersson, J. Yuan, B. Sundén, Sofc modeling considering electrochemical reactions at the active three phase boundaries, International Journal of Heat and Mass Transfer 55 (4) (2012) 773–788.

[102] S. B. Beale, M. Andersson, C. Boigues-Muñoz, H. L. Frandsen, Z. Lin, S. J. McPhail, M. Ni, B. Sundén, A. Weber, A. Z. Weber, Continuum scale modelling and complementary experimentation of solid oxide cells, Progress in Energy and Combustion Science 85 (2021) 100902.

[103] S. Ubertini, R. Bove, Mathematical Models: A General Overview, Springer Netherlands, Dordrecht, 2008, pp. 51–93.

[104] D. Noren, M. Hoffman, Clarifying the butler–volmer equation and related approximations for calculating activation losses in solid oxide fuel cell models, Journal of Power Sources 152 (2005) 175–181.

[105] B. Sundén, Hydrogen, batteries and fuel cells, Academic Press, 2019.

[106] P. Aguiar, C. Adjiman, N. Brandon, Anode-supported intermediate temperature direct internal reforming solid oxide fuel cell. i: model-based steady-state performance, Journal of Power Sources 138 (1) (2004) 120–136.

[107] E. J. Dickinson, A. J. Wain, The butler-volmer equation in electrochemical theory: Origins, value, and practical application, Journal of

Electroanalytical Chemistry 872 (2020) 114145, dr. Richard Compton 65th birthday Special issue.

[108] S. Adler, Chapter 11: Sources of cell and electrode polarization losses in sofcs, in: K. Kendall, M. Kendall (Eds.), High-Temperature Solid Oxide Fuel Cells for the 21st Century (Second Edition), second edition Edition, Academic Press, Boston, 2016, pp. 357–381. doi:https://doi.org/10.1016/B978-0-12-410453-2.00002-6.

[109] N. Eliaz, E. Gileadi, Physical electrochemistry: fundamentals, techniques, and applications, John Wiley & Sons, 2019.

[110] G. Kaur, Sofc technology: Its working and components, in: Solid Oxide Fuel Cell Components, Springer, 2016, pp. 79–122.

[111] T. Yonekura, Y. Tachikawa, T. Yoshizumi, Y. Shiratori, K. Ito, K. Sasaki, Exchange current density of solid oxide fuel cell electrodes, ECS Transactions 35 (1) (2011) 1007.

[112] K. Takino, Y. Tachikawa, K. Mori, S. Lyth, Y. Shiratori, S. Taniguchi, K. Sasaki, Simulation of sofc performance using a modified exchange current density for pre-reformed methane-based fuels, International Journal of Hydrogen Energy 45 (11) (2020) 6912–6925.

[113] J. Ferguson, J. M. Fiard, R. Herbin, Three-dimensional numerical simulation for various geometries of solid oxide fuel cells, Journal of Power Sources 58 (2) (1996) 109–122.

[114] D. Kanno, N. Shikazono, N. Takagi, K. Matsuzaki, N. Kasagi, Evaluation of sofc anode polarization simulation using three-dimensional microstructures reconstructed by fib tomography, Electrochimica Acta 56 (11) (2011) 4015–4021.

[115] J. O. Bockris, A. K. Reddy, M. E. Gamboa-Aldeco, Modern electrochemistry 2B: electrodics in chemistry, engineering, biology and environmental science, Vol. 2, Springer Science & Business Media, 1998.

[116] A. Comsol, Cfd modules user' s guide, comsol multiphysics v. 5.4, COMSOL AB, Stockholm, Sweden.

[117] M. Andersson, J. Yuan, B. Sundén, Sofc modeling considering hydrogen and carbon monoxide as electrochemical reactants, Journal of Power Sources 232 (2013) 42–54.

[118] C. Curtiss, R. B. Bird, Multicomponent diffusion, Industrial & Engineering Chemistry Research 38 (7) (1999) 2515–2522.

[119] R. C. Reid, J. M. Prausnitz, B. E. Poling, The properties of gases and liquids.

[120] S. Zeng, M. Xu, J. Parbey, G. Yu, M. Andersson, Q. Li, B. Li, T. Li, Thermal stress analysis of a planar anode-supported solid oxide fuel cell: Effects of anode porosity, International Journal of Hydrogen Energy 42 (31) (2017) 20239–20248.

[121] E. N. Fuller, P. D. Schettler, J. C. Giddings, New method for prediction of binary gas-phase diffusion coefficients, Industrial & Engineering Chemistry 58 (5) (1966) 18–27.

[122] Justifying the significance of knudsen diffusion in solid oxide fuel cells, Energy 95 (2016) 242–246.

[123] J. Yuan, Y. Huang, B. Sundén, W. G. Wang, Analysis of parameter effects on chemical reaction coupled transport phenomena in sofc anodes, Heat and Mass Transfer 45 (4) (2009) 471–484.

[124] M. Andersson, X. Lu, J. Yuan, B. Sundén, Analysis of microscopic anode structure effects on an anode-supported sofc including knudsen diffusion, ECS Transactions 35 (1) (2011) 1799.

[125] B. Todd, J. Young, Thermodynamic and transport properties of gases for use in solid oxide fuel cell modelling, Journal of Power Sources 110 (1) (2002) 186–200.

[126] W. Minkowycz, A. Haji-Sheikh, K. Vafai, On departure from local thermal equilibrium in porous media due to a rapidly changing heat source: the sparrow number, International Journal of Heat and Mass Transfer 42 (18) (1999) 3373–3385.

[127] A. Amiri, K. Vafai, Transient analysis of incompressible flow through a packed bed, International Journal of Heat and Mass Transfer 41 (24) (1998) 4259–4279.

[128] A. Bejan, Convection heat transfer, John wiley & sons, 2013.

[129] H. S. Spacil, Electrical device including nickel-containing stabilized zirconia electrode, uS Patent 3,503,809 (Mar. 31 1970).

[130] F. Wang, H. Kishimoto, T. Ishiyama, K. Develos-Bagarinao, K. Yamaji, T. Horita, H. Yokokawa, A review of sulfur poisoning of solid oxide fuel cell cathode materials for solid oxide fuel cells, Journal of Power Sources 478 (2020) 228763.

[131] L. Zhou, J. H. Mason, W. Li, X. Liu, Comprehensive review of chromium deposition and poisoning of solid oxide fuel cells (sofcs) cathode materials, Renewable and Sustainable Energy Reviews 134 (2020) 110320.

[132] B. Shri Prakash, S. Senthil Kumar, S. Aruna, Properties and development of ni/ysz as an anode material in solid oxide fuel cell: A review, Renewable and Sustainable Energy Reviews 36 (2014) 149–179.

[133] S. Afroze, A. Karim, Q. Cheok, S. Eriksson, A. K. Azad, Latest development of double perovskite electrode materials for solid oxide fuel cells: a review, Frontiers in Energy 13 (4) (2019) 770–797.

[134] J. R. Wilson, W. Kobsiriphat, R. Mendoza, H.-Y. Chen, J. M. Hiller, D. J. Miller, K. Thornton, P. W. Voorhees, S. B. Adler, S. A. Barnett, Three-dimensional reconstruction of a solid-oxide fuel-cell anode, Nature materials 5 (7) (2006) 541–544.

[135] J. R. Izzo, A. Joshi, K. Grew, W. Chiu, A. Tkachuk, S. Wang, W. Yun, Nondestructive reconstruction and analysis of solid oxide fuel cell anodes using x-ray computed tomography at sub-50 nm resolution, ECS Transactions 13 (6) (2008) 1.

[136] J. Irvine, J. L. Rupp, G. Liu, X. Xu, S. Haile, X. Qian, A. Snyder, R. Freer, D. Ekren, S. Skinner, et al., Roadmap on inorganic perovskites for energy applications, Journal of Physics: Energy 3 (3) (2021) 031502.

[137] L. Mahmud, A. Muchtar, M. Somalu, Challenges in fabricating planar solid oxide fuel cells: A review, Renewable and Sustainable Energy Reviews 72 (2017) 105–116.

[138] Z. Zakaria, Z. Awang Mat, S. H. Abu Hassan, Y. Boon Kar, A review of solid oxide fuel cell component fabrication methods toward lowering temperature, International Journal of Energy Research 44 (2) (2020) 594–611.

[139] M. J. Martínez, S. Shimpalee, J. Van Zee, Measurement of macmullin numbers for pemfc gas-diffusion media, Journal of The Electrochemical Society 156 (1) (2008) B80.

[140] M. Andersson, S. Beale, M. Espinoza, Z. Wu, W. Lehnert, A review of cell-scale multiphase flow modeling, including water management, in polymer electrolyte fuel cells, Applied Energy 180 (2016) 757–778.

[141] O. M. Pecho, O. Stenzel, B. Iwanschitz, P. Gasser, M. Neumann, V. Schmidt, M. Prestat, T. Hocker, R. J. Flatt, L. Holzer, 3d microstructure effects in ni-ysz anodes: Prediction of effective transport properties and optimization of redox stability, Materials 8 (9) (2015) 5554–5585.

[142] B. Tjaden, D. J. Brett, P. R. Shearing, Tortuosity in electrochemical devices: a review of calculation approaches, International Materials Reviews 63 (2) (2018) 47–67.

[143] B. Ghanbarian, A. G. Hunt, R. P. Ewing, M. Sahimi, Tortuosity in porous media: a critical review, Soil science society of America journal 77 (5) (2013) 1461–1477.

[144] Tortuosity characterization of 3d microstructure at nano-scale for energy storage and conversion materials, Journal of Power Sources 249 (2014) 349–356.

[145] On tortuosity and the tortuosity factor in flow and diffusion through porous media, Chemical Engineering Science 44 (3) (1989) 777–779.

[146] W. He, J. Zou, B. Wang, S. Vilayurganapathy, M. Zhou, X. Lin, K. H. Zhang, J. Lin, P. Xu, J. H. Dickerson, Gas transport in porous electrodes of solid oxide fuel cells: A review on diffusion and diffusivity measurement, Journal of Power Sources 237 (2013) 64–73.

[147] B. Tjaden, S. J. Cooper, D. J. Brett, D. Kramer, P. R. Shearing, On the origin and application of the bruggeman correlation for analysing transport phenomena in electrochemical systems, Current Opinion in Chemical Engineering 12 (2016) 44–51, nanotechnology / Separation Engineering.

[148] I. V. Thorat, D. E. Stephenson, N. A. Zacharias, K. Zaghib, J. N. Harb, D. R. Wheeler, Quantifying tortuosity in porous li-ion battery materials, Journal of Power Sources 188 (2) (2009) 592–600.

[149] R. Millington, J. Quirk, Permeability of porous solids, Transactions of the Faraday Society 57 (1961) 1200–1207.

[150] J. Hoogschagen, Diffusion in porous catalysts and adsorbents, Industrial & Engineering Chemistry 47 (5) (1955) 906–912.

[151] S. Pawlowski, N. Nayak, M. Meireles, C. Portugal, S. Velizarov, J. Crespo, Cfd modelling of flow patterns, tortuosity and residence time distribution in monolithic porous columns reconstructed from x-ray tomography data, Chemical Engineering Journal 350 (2018) 757–766.

[152] M. Zare, S. H. Hashemabadi, Cfd simulation and experimental validation of tortuosity effects on pellet-fluid heat transfer of regularly stacked multi-lobe particles, Chemical Engineering Journal 361 (2019) 1543–1556.

[153] S. Cooper, A. Bertei, P. Shearing, J. Kilner, N. Brandon, Taufactor: An open-source application for calculating tortuosity factors from tomographic data, SoftwareX 5 (2016) 203–210.

[154] M. Andersson, H. Nakajima, T. Kitahara, A. Shimizu, T. Koshiyama, H. Paradis, J. Yuan, B. Sundén, Comparison of humidified hydrogen and partly pre-reformed natural gas as fuel for solid oxide fuel cells applying computational fluid dynamics, International Journal of Heat and Mass Transfer 77 (2014) 1008–1022.

[155] Y. Su, Z. Zhong, Z. Jiao, A novel multi-physics coupled heterogeneous single-cell numerical model for solid oxide fuel cell based on 3d microstructure reconstructions, Energy & Environmental Science 15 (6) (2022) 2410–2424.

[156] W. Ming, P. Sun, Z. Zhang, W. Qiu, J. Du, X. Li, Y. Zhang, G. Zhang, K. Liu, Y. Wang, et al., A systematic review of machine learning methods applied to fuel cells in performance evaluation, durability prediction, and application monitoring, International Journal of Hydrogen Energy 48 (13) (2023) 5197–5228.

[157] Z. Niu, W. Zhao, B. Wu, H. Wang, W.-F. Lin, V. J. Pinfield, J. Xuan, π learning: A performance-informed framework for microstructural electrode design, Advanced Energy Materials (2023) 2300244.

Summary of publications

Author contributions

Paper I: Thermal stress analysis at the interface of cathode and electrolyte in solid oxide fuel cells

Xiaoqiang Zhang contributes to model building and modeling operation and process data; Siqi Yu contributes to draw figures and edit figures; Minkang Wang contributes to the introduction writing; Shuyue Dong contributes to model modification and improve its accuracy; Joseph Parbey contributes to the English editing and grammar editing; Martin Andersson offers help in model building and explanations on results; Tingshuai Li proposes the problems to solve and addresses the draft to improve its quality in all aspects.

Paper II: Numerical simulation of solid oxide fuel cells comparing different electrochemical kinetics

Xiaoqiang Zhang contributes to the development and operation of the model building, data processes and the first draft; Lei Wang, Tingshuai Li, and Mayken Espinoza contribute to the editing of the manuscript, data analysis. Martin Andersson provide help on data analyses, draft revision and supervision.

Paper III: Parametric study for electrode microstructure influence on SOFC performance

Xiaoqiang Zhang contributes to the development and operation of the model building, data processes and the first draft; Mayken Espinoza and Tingshuai Li contribute to manuscript editing and data analysis. Martin Andersson provided help with data analysis, draft revision, and supervision.

Paper IV: Analysing Tortuosity for Solid Oxide Fuel Cell Anode

Material - Experiments and Modeling

Xiaoqiang Zhang contributes to the fuel cell test, 3D reconstruction, data analysis and the first manuscript; Danan Yang helped with data extraction; Aaron Naden helped with electrode characterization; Min Xu contributes to data analysis, manuscript editing; Tingshuai Li contributes to manuscript editing data analyzing; John Irvine provided the experimental laboratory and data analysis; Martin Andersson provided help with improving manuscript quality and overall supervision.

Paper V: High gas tightness ZrO_2 doped silicate glass sealant with low thermal stress for solid oxide fuel cells

Mengyuan Guo: Conceptualization, Methodology, Investigation, Formal analysis, Data curation, Visualization, Writing-original draft. Xiaoqiang Zhang: Conceptualization, Methodology, Investigation, Formal analysis, Data curation, Visualization, Writing-original draft. Ying Li, Data curation, Visualization. Martin Andersson: Data curation, Visualization, Validation, Writing-review and editing, Supervision, Project administration, Funding acquisition. Zhibin Yang: Data curation, Visualization, Validation, Writing - review and editing, Supervision, Project administration, Funding acquisition. Suping Peng: Resources, Funding acquisition.

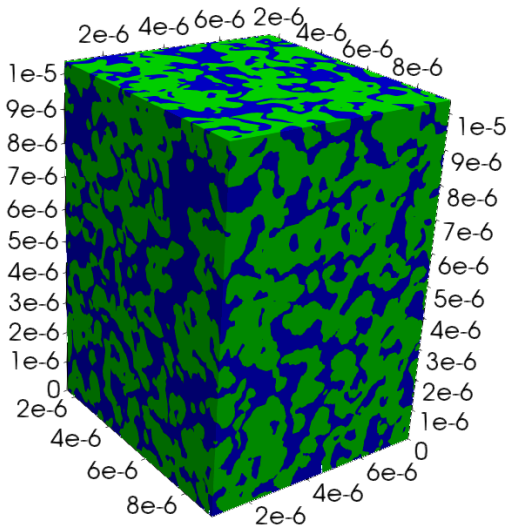

In SOFC simulations, a heterogeneous porous structure is often simplified as a homogeneous bulk material with effective properties. Considering microstructure optimization, the real geometry as shown above is needed to quantitatively assess the porous electrode performance. The real geometry also can be used to derivate the effective properties for a more accurate SOFC simulation.

Printed by Media-Tryck, Lund 2023 NORDIC SWAN ECOLABEL 3041 0903

LUND UNIVERSITY

Faculty of Engineering
Department of Energy Sciences

ISBN: 978-91-8039-729-2
ISSN: 0282-1990
ISRN: LUTMDN/TMHP-23/1174-SE